An archaeomagnetic intensity-based search for order in the chaos of the destruction of Hama (Syria) dated to 720 BCE

Yves Gallet, Georges Mouamar, Stephen Lumsden, Mette Marie Hald

An archaeomagnetic intensity-based search for order in the chaos of the destruction of Hama (Syria) dated to 720 BCE

Yves Gallet[1], Georges Mouamar[2,3], Stephen Lumsden[2], Mette Marie Hald[2]

[1] Université Paris Cité, Institut de physique du globe de Paris, CNRS, F-75005 Paris, France

[2] National Museum of Denmark, Copenhagen, Denmark

[3] Institut Français du Proche-Orient

Abstract

Destruction layers of ancient settlements are extremely valuable for archaeomagnetic studies as they provide a particular archaeological context allowing for the analysis of ceramic fragments strongly linked to the date of destruction. However, when examining pottery for archaeomagnetic intensity, instead of considering a snapshot in time in the geomagnetic field record, we must also consider the various dates of their initial production, which can span several decades. This introduces an unknown time interval, which is typically shorter than the temporal resolution offered by pottery typology. In this study, we obtained new archaeomagnetic intensity data using the Triaxe protocol from 16 fragments (77 specimens) of different ceramics recovered from the destruction layer of Hama (Syria) dated to 720 BCE, caused by the troops of the Assyrian King Sargon II. The selected pottery consists of serving vessels, which are generally thought to have a short lifespan, all of which were found in royal or other important buildings. Our results reveal a significant scatter, ranging from ~65 μT to ~81 μT (average 74.2 ± 4.2 μT). We attribute this dispersion mainly to the time interval for the production of the pottery during the 8th century BCE, a period marked by rapid intensity fluctuations according to the currently available reference geomagnetic field intensity variation curve for the Near East. Using this curve, we show that the ceramics studied had

been in use for at least 30 years at the time of the city's destruction, a surprisingly long use-life for ceramics intended for everyday use. While we acknowledge a 30-years use-life as possible, we suggest that this minimum time interval could be a result of inaccuracies in the reference intensity variation curve during the 8th century BCE. Nevertheless, our study illustrates and confirms the ability of pottery from a destruction layer to trace rapid variations in geomagnetic field intensity. Furthermore, it establishes a chronological order of production date in ceramic assemblages found in an otherwise chaotic context.

Keywords : Archaeointensity, Archaeomagnetic Dating, Chronology, Pottery, Destruction layer

1. Introduction

As early as the pioneering works of Giuseppe Folgheraiter, Paul-Louis Mercanton, Pierre David and Bernard Brunhes in the late 19th and early 20th centuries, the application of the magnetic properties of archaeological artifacts to answer archaeological questions was envisioned and very partially explored (see, for example, the discussion by Gallet, 2021). Recently, archaeomagnetism research has witnessed remarkable progress, enabling for certain regions the establishment of rather detailed directional and/or intensity secular variation curves of the Earth's magnetic field over the past few millennia. The accuracy of these records is constantly improving (Brown et al., 2015; 2021). As a result, it has become relatively common practice in archaeology to use temporal variations in the geomagnetic field as a dating tool for artifacts with thermoremanent magnetization, i.e. those that have been fired during manufacture or use (e.g., kilns, bricks, pottery; Le Goff et al., 2002; Pavón-

48 Carrasco et al., 2011; Schnepp et al., 2015; Hervé and Lanos, 2017; Gallet and Le Goff, 2023;
49 Genevey et al., 2021).

50 While the direction of magnetization of objects found away from the place where they
51 were initially fired during manufacture cannot be utilized for dating purposes, unless
52 assumptions can be made about their position during firing, information regarding
53 geomagnetic intensities still remains useful. Based on newly constructed curves of
54 geomagnetic field intensity variations, particularly for Western Europe and the Near East, the
55 archaeointensity-based dating method is rapidly expanding (e.g., Shaar et al., 2020; Genevey
56 et al., 2021; Gallet et al., 2020; 2021). Archaeomagnetists explore a variety of archaeological
57 contexts, including destruction levels uncovered in ancient settlements.

58 Destruction levels serve as valuable chronological markers for archaeology at both
59 local and regional levels. Often, they provide numerous artifacts in a contemporary context,
60 sealed by the destruction event. Such a situation is particularly interesting for
61 archaeomagnetism, especially in the Near East where many archaeological sites are multi-
62 layered, with occupation sequences sometimes extending over several millennia. Destruction
63 levels allow archaeomagnetists to obtain ceramic samples that are contemporary in time, or at
64 least share a common *terminus ante quem*. This is particularly true for burnt levels, where
65 sun-dried architectural bricks become fired, with the resulting thermoremanent magnetization
66 dating very precisely to the burning. This was illustrated by Vaknin et al (2022) for sites in
67 the southern Levant ravaged and burned by Assyrian and then Babylonian troops during the
68 first half of the 1st millennium BCE, both events recorded and dated in the Old Testament
69 (see also Shahack-Gross et al., 2018; Vaknin et al., 2020).

70 The case of pottery is different because in addition to the *terminus ante quem* given by
71 the date of destruction, we must consider the period during which the ceramics found in the
72 destruction level were first produced and then used, which could extend over several decades.

This timeframe is often shorter than the temporal resolution offered by studies of ceramic typology. Such pottery can provide valuable insights into rapid variations in geomagnetic field intensities, as argued by Shaar et al. (2016) for sets of common, locally made pottery from Tel Megiddo and Tel Hazor, two sites in the Southern Levant destroyed by the troops of the Assyrian King Tiglath-Pileser III in 732 BCE. However, we question the fact that the archaeointensity values obtained from these ceramics exhibit significant differences, some more extreme than others. One would expect a more gradual continuum of intensity values, reflecting the chronological progression from the oldest pottery to those most contemporary with the destruction level. In principle, this continuum or these differences would allow the pottery to be placed in chronological order once a detailed reference curve of geomagnetic intensity variations for the period under consideration is available. The Near East, particularly the Levant region during the first half of the 1st millennium BCE, offers favorable conditions for such endeavors. Numerous archaeomagnetic studies have been conducted in this region in recent years, providing a large set of archaeointensity data (e.g. Gallet and al-Maqdissi, 2010; Gallet et al., 2006; Shaar et al., 2016; 2021; 2022; Livermore et al., 2021). Consequently, from the chaos caused by the violent destruction of a site, it becomes possible to establish, with archaeomagnetism, a comparative chronology for the manufacture of the ceramics discovered in the rubble.

As an example of this application, we have chosen to work on the destruction level of the important city of Hama (ancient Hamath), in the western part of modern Syria (Northern Levant). This destruction was caused by troops of the Assyrian King Sargon II in 720 BCE, around ten years after the destruction of Tel Megiddo and Tel Hazor, located further south. During this historical event, royal and other official buildings were totally destroyed. Discoveries of molten basalt pellets, signaling temperatures exceeding ~1200 °C, provided

97 compelling evidence of an intense fire. The level of rubble reached a thickness of several
98 dozen centimeters (Fugmann, 1958).

99 The mound at Hama was excavated in the 1930s by a team of Danish archaeologists
100 under the direction of Harald Ingholt (Ingholt, 1934; 1940; Fugmann, 1959; Riis and Buhl,
101 1990). These excavations were carried out at a fairly high scientific level for the time period,
102 meeting most modern excavation criteria, and a substantial portion of the discovered artifacts
103 was carefully catalogued and preserved in the National Museum of Denmark in Copenhagen.
104 Taking advantage of these conditions, our study has focused on a large series of fragments,
105 each originating from a distinct ceramic vessel found in the 720 BCE destruction layer. Our
106 aim was to trace the detailed evolution of geomagnetic intensities during the decades
107 preceding 720 BCE and, at the same time, attempt to establish the chronology of the studied
108 ceramics relative to one another. To some extent, our study presents a methodological aspect
109 from the perspective of archaeomagnetism research. However, it is important to note that the
110 inferences discussed below may vary depending on the destruction layers studied, as each site
111 has unique characteristics that may differ from one to another, and on the fluctuating nature of
112 the geomagnetic field intensities.

113

114 **2. Archaeological context and sampling**

115 The mound at Hama (λ = 35°N 08' 07.5'', ϕ = 36°E 44' 59.0''; Fig. 1a), around which the
116 modern city has developed, is located within a meander of the Orontes River in inland
117 western Syria, ~185 km north of Damascus and ~125 km south of Aleppo. It measures ~430
118 meters in length, ~300 meters in width and ~46 meters in height. The archaeological
119 excavations unveiled a lengthy sequence of occupation spanning nearly 8000 years of history,
120 from the Neolithic to the Ottoman period. The archaeological deposits were classified into

twelve phases, designated A to M. Our focus is on Phase E, which corresponds to the Iron Age II Period spanning from ~950-900 to 720 BCE (Fugmann, 1958; Riis and Buhl, 1990; Lumsden, 2019). This period marked a time of prosperity for the city, as Hamath was the southernmost of the Syro-Hittite kingdoms, exerting control over a significant portion of west-central Syria.

The excavations of the Iron Age buildings in the 'Royal Quarter' took place between 1935 and 1938. Four important buildings (I-IV) were unearthed, arranged around a spacious plaza (Fig. S1). Building I served as a grand gateway providing access to the monumental buildings of the Royal Quarter. Building II, situated on an elevated position on the western edge of the mound, is the largest structure that was discovered, possibly functioning as the royal palace. The lower-floor rooms found in this building primarily served as storage spaces, with many vessels found *in situ* (Fig. 1b). Building III, located across the plaza from Building II, was another substantial building that remained only partially excavated. Building IV seems to have served as a gateway connecting the Royal Quarter to the elevated part of the city on the mound. All of these buildings appear to have been adorned with basalt lion gate guardian figures, as detailed by Fugmann (1958).

Remnants of Phase E were also recovered in other areas of the mound, extending beyond the monumental Royal Quarter. Although only partially excavated, Building V, situated at the western edge of the mound, was obviously an important building, possibly a royal palace. It yielded a rich assemblage of artifacts, including weapons, imported ceramics, bone inlays for furniture, sealed bullae, and ivory furniture inlays, all of which attest to the significance of the building. In square K15, located at the eastern edge of the mound, walls with the same alignment as those of Building III and fragments of basalt sculpture were found, suggesting a possible northward extension of the aforementioned building. In the center of the mound, within a large excavation unit where layers from the Bronze Age and

earlier periods were uncovered (squares I9-10), and directly above what the excavators described as a Late Bronze Age palace, fragmentary walls and carved basalt elements (lion and possibly sphinx gate guardian figures) were also discovered, probably indicating the existence of another monumental building from Phase E in this part of the town.

All the buildings of phase E were looted and extensively burned in an event that marked the end of this archaeological phase. This event, which completely destroyed buildings I-IV, is associated with the conquest of the Hamath kingdom by the troops of Sargon II in 720 BCE. It was a response to the region's uprising, led by Ilu-bidi of Hamath, against Assyrian domination. Several texts mention the destruction of the kingdom of Hamath during Sargon II's military campaign in 720 BCE, resulting in the loss of its independence and its integration into the Assyrian provincial system. Other evidence for this event includes a carved relief from Sargon's palace at Khorsabad that depicts Ilu-bidi being flayed alive (Botta and Flandin, 1849). However, no text directly links the destruction of the city of Hama to this campaign (see discussion in Baaklini, 2019). Nevertheless, the systematic and extensive destruction revealed by archaeological excavations, the dating of the ceramics found in context, and the historical context based on Assyrian chronicles provide convincing evidence for a destruction in 720 BCE. According to the evidence of the excavations, the extent of the destruction of Hama was so severe that the city remained largely deserted until the Hellenistic period (around the 2nd century BCE).

The rubble resulting from the destruction of Hama forms a thick layer from which the large pottery fragments analyzed in our study originated (Fig. 2). These fragments were found on the floors of different rooms in the monumental buildings, ensuring their contemporaneity with the destruction event. We specifically selected fragments without clear or visible signs of reheating, found in areas of the site where the fire seemed to have been less intense. Additionally, we excluded fragments from cooking pots and deliberately avoided large

storage vessels that might have been used for decades in the storage rooms. The majority of the ceramics sampled for this study consisted of serving vessels, which were likely to have had a relatively short use-life. These ceramics include the local *Common Ware* and *Red Slip Ware*, which form a very homogenous assemblage dating to the Iron Age II. It is characterized by a significant increase in open shapes. The *Common Ware* is represented by open forms, including a variety of undecorated and painted bowls, footed and painted bowls, painted platters, and painted flasks. Examples of *Red Slip Ware* include red polished, footed platter/fruit stands, footed *Red Slip* bowls and red polished platters. This ceramic assemblage can be attributed to the 8th century BCE when Hamath was ruled by kings with Aramean names. It is as yet not possible to establish a relative chronology of the analyzed ceramic wares based on their typology alone.

Lastly, it is important to mention that the common pottery studied here, intended for everyday use, without specific form, sophisticated craftsmanship or elaborate decoration, was produced locally, if not in Hama itself, at least in its immediate vicinity. As a major urban and royal center, Hama had no need to import common ceramics from distant pottery manufacturing sites. This is particularly true if we consider that the cost and difficulty of transport would have been at odds with their practical use, especially in a region where clay sources were ubiquitous. A few fragments of fine, decorated, high-quality ceramics imported from Cyprus and Greece were found in the destruction layer of phase E (Fugmann, 1958), and these fragments are easily distinguished from the common ceramics. Furthermore, preliminary petrographic and chemical analyses reveal a good degree of homogeneity in the clays used for pottery production throughout Hama's history (work in progress). More specifically, for Phase E, the clay used for adobe and baked brick production, which is clearly of local origin, shows similarities with the clay used for pottery production.

196 **3. Archaeointensity method and results**

197 The archaeointensity measurements were carried out using Triaxe magnetometers,
198 which are laboratory-built vibrating sample magnetometers. These magnetometers measure
199 the magnetization carried by a small-volume specimen (~0.7 cm^3) directly at high
200 temperatures up to 650 °C, with increments of ~5 °C, in zero field or in a field of up to 200
201 μT in any direction (Le Goff and Gallet, 2004). The experimental protocol developed for the
202 Triaxe has been described elsewhere (e.g., Gallet and Le Goff, 2006; Genevey et al., 2009;
203 Hartmann et al., 2010; Gallet et al., 2022) and we will only highlight its main features below.

204 The analysis involves setting two reference temperatures determined by the
205 experimenter. T1 is generally chosen at 150 °C in order to exclude a part of the remanent
206 magnetization of viscous origin. T2 is set at around 500 °C to allow for the demagnetization
207 of the major part of the natural remanent magnetization (NRM), i.e. the thermoremanent
208 magnetization (TRM) acquired during the initial firing of the ceramic vessel, and the
209 thermoremanent magnetization acquired in a laboratory field (TRM_{lab}). The direction of the
210 laboratory field is automatically adjusted so that TRM_{lab} is parallel to NRM, and its intensity
211 (H_{lab}) is set by the experimenter.

212 From a succession of five series of measurements between T1 and T2 (see a detailed
213 description of the procedure in Le Goff and Gallet, 2004), intensity values are obtained for a
214 specimen by considering the ratio of the NRM and TRM_{lab} magnetization fractions isolated
215 between T1 and a progressively increasing temperature Ti, and multiplying it by H_{lab}. The
216 resulting values, known as the R'(Ti) dataset, are estimated between T1 and T2 and should
217 remain fairly constant over the entire range of analysis temperatures. However, if a secondary
218 magnetic component is present at temperatures >T1, the range can be reduced between T1'
219 (with T1'>T1) and T2 . The arithmetic mean of the R'(Ti) data gives the characteristic
220 intensity value of the specimen under study.

We note that the R'(Ti) data do not require correction for a potential TRM anisotropy effect because the direction of TRM_{lab} is precisely parallel to that of the primary NRM component used for intensity determination. It has also been shown experimentally that the R'(Ti) data are minimally affected by the cooling rate effect on TRM acquisition (e.g., Le Goff and Gallet, 2004; Genevey et al., 2009; Hartmann et al., 2010; 2011; Gallet et al., 2022). This effect generally prevents the determination of intensity values using the ratio of NRM to TRM_{lab} fractions that remain unblocked between Ti and T2, as it primarily affects magnetic grains with high unblocking temperatures. Determined between T1 (or T1') and T2, and after their multiplication by H_{lab}, these values define the R(Ti) dataset. It is worth noting that the R(Ti) and R'(Ti) data are very close to each other when the cooling rate effect is negligible. To further minimize the potential impact of cooling rate on TRM acquisition, we systematically used a cooling rate of 10 °C/minute for TRM_{lab} acquisition in our study, instead of the 2 °C/minute rate routinely used so far (Gallet et al., 2022).

Recently, Gallet et al. (2022) introduced a new parameter, called AutoR'(Ti). This parameter calculates the mean R'(Ti) values obtained by progressively reducing the temperature range from T1'-T2 to T2'-T2, with T2' = T2 – 50 °C, ensuring that the averages of the R'(Ti) values are based on at least 10 values. It is used to verify the stability of intensity estimates across the entire temperature range, indicating minimal dependence on the specific choice of T1'. These estimates rely solely on the primary NRM component.

A total of approximately 70 fragments, each from a different pot, were measured. However, only 16 yielded archaeointensity results that met the selection criteria defined for the Triaxe data (e.g. Gallet and Le Goff, 2006; Genevey et al., 2009, see for example Table 1 in Gallet et al., 2022). The magnetic mineralogy of these fragments was studied using isothermal remanent magnetization (IRM) acquisition curves up to 1.5 T (Fig. S2), thermal demagnetization of three orthogonal IRM acquired in 1.5 T, 0.4 T and 0.2 T fields (Fig. S3;

246 Lowrie, 1990), and heating-cooling cycles of low field magnetic susceptibility measured
247 between room temperature and ~620 °C (Fig. S2). These experiments indicate that the
248 magnetization is predominantly carried by low-coercivity (0.2 T) minerals with unblocking
249 temperatures below 600 °C, which is consistent with the presence of (titano)magnetite. The
250 IRM measurements also reveal the presence of a small fraction of high-coercivity minerals
251 with unblocking temperatures lower than 600 °C, which are probably fine-grained hematite.
252 We note that this dual magnetic mineralogy seems to be fairly widespread in Near Eastern
253 and Central Asian baked-clay artefacts regardless of their age (e.g., Gallet et al., 2020;
254 Troyano et al., 2021).

255 For Triaxe measurements, up to seven specimens were prepared by drilling or sawing
256 from each fragment, resulting in the successful analysis of 77 specimens. Most fragments
257 exhibit a secondary magnetization component up to ~300 °C, probably associated with the
258 fire that occurred during Hama's destruction. The rejection of the other potsherds primarily
259 stems from the persistence of this secondary component at temperatures too high to allow for
260 an accurate determination of the intensity characteristics of the primary NRM component.

261 An important characteristic of the suitable potsherds' magnetic behavior is the
262 apparent absence of a cooling rate effect on TRM acquisition. As mentioned earlier, this
263 results in remarkably similar R(Ti), R'(Ti) and AutoR'(Ti) values for each of the studied
264 specimens across the entire range of temperatures selected for archaeointensity determinations
265 (four examples are shown in Fig. 3). Despite the close proximity of these values, we base our
266 obtained archaeointensity values solely on the R'(Ti) data, following the conventional
267 approach with Triaxe data. In our study, each fragment is represented by a minimum of three
268 specimens, but in most cases we have five specimens (14 of 16; Table 1). Six examples of
269 R'(Ti) data obtained from different specimens of the same fragment are shown in Fig. 4
270 (Table S1; all other data are shown in Fig. S4). An intensity value per fragment is thus

obtained by averaging the intensity values of the different specimens, which are themselves the averages of the R'(Ti) values for each specimen over the temperature range T1'-T2.

Each archaeointensity value at the fragment level exhibits a dispersion (standard deviation) of less than 5% around the mean (in accordance with one of the selection criteria used). This scatter, illustrated by the different diagrams of Fig. 4 and S4, ranges from 0.6 μT (0.8%) to 3.6 μT (4.8%) with a median of 1.5 μT (Tables 1, S2). Furthermore, the mean intensity values at the fragment level vary from 64.8 ± 2.2 μT to 80.8 ± 0.8 μT (Fig. 5). These differences are significant, even though the mean intensity value obtained from all fragments (74.2 ± 4.2 μT) is defined with a dispersion value (5.7% of the mean value) that is typical and representative of archaeointensity data (e.g. Genevey et al., 2008; Brown et al., 2015). When the uncertainties obtained at the fragment level are propagated to the level of all fragments, this dispersion increases to 4.5 μT (6.0%) (see discussion in Gallet et al., 2022). It is important to note that the scatter we are discussing includes two components: one related to the efficiency of the protocol used and the recording process, and the other associated with the date of pottery production relative to the geomagnetic intensity variations during that period. Here, we can reasonably assume that the latter component dominates the former. This assumption is supported by the histogram of archaeointensity values obtained per fragment (diagram on the right, Fig. 5), which displays a relatively broad distribution, although the null hypothesis that the intensity data are normally distributed cannot be rejected at the 95% confidence level according to the Shapiro-Wilk normality test (p-value=0.7111, W=0.9627).

4. Discussion

The evolution of geomagnetic field intensities during the first half of the 1st millennium BCE, particularly during the 8th century BCE, is now documented through a large

dataset primarily obtained from archaeological sites in the Southern Levant (e.g. Shaar et al., 2016; 2022; Vaknin et al., 2022). Some data also come from the Northern Levant and Mesopotamia (Gallet et al., 2006; Gallet and al-Maqdissi, 2010 Livermore et al., 2021). An archaeointensity variation curve was calculated using the Bayesian AH-RJMCMC (for Age Hyper-parameter Monte Carlo Markov Chain) method developed by Livermore et al. (2018). In this method, the data are fitted along linear segments whose number and position are defined by the data themselves, without any prior assumption on the nature of the expected variations (for a detailed description of the method, see Livermore et al., 2018). The intensity variation curve computed using the data compilation by Shaar et al. (2022) is presented in Fig. 6a (referred to as LAC in Shaar et al., 2022; computational parameters are indicated in the figure caption; Table S3). Note that the curve calculations enable the recovery of the probability density functions (pdf) of the intensity values defining the reference curve. These pdf, shown in Fig. 6 using a grey color code, are used for correlation dating (see below). The curve exhibits a succession of four intensity peaks, known as geomagnetic spikes (Shaar et al., 2022), with rates of change exceeding 0.25 μT/year. The 8th century BCE is characterized by an intensity maximum occurring during the second half of this century, while the first half shows a significant increase in intensity with an amplitude of ~12 μT (between ~75 μT and 87 μT). This evolution serves as a basis for discussing the results obtained for the destruction layer of Hama dated to 720 BCE.

The new Hama data, derived from the average of all fragments (close red dot), as well as individual fragments (open red dots), are also reported in Fig. 6. These data are arbitrarily placed within a time interval of 30 years before 720 BCE (between 750 and 720 BCE) due to their probable short use-life. A discrepancy becomes apparent when comparing this rough dating with the current intensity variation curve, since the Hama data significantly deviate from the values of the reference curve. This inconsistency is highlighted by the dating of the

fragment-group intensity value correlated across a wide time interval between 850 and 720 BCE. With this approach, the pdf of the intensity value to be dated (i.e., Gaussian) is multiplied by the (non-Gaussian) pdf of the intensity values forming the reference curve, resulting in the pdf of the age of the ceramics (e.g., Genevey et al., 2021). The outcome indicates two dating intervals at the 95% probability level between ~850 and 843 BCE, and between ~838 -758 BCE, i.e. ~40 years prior to the destruction of Hama by the troops of Sargon II (Fig. 7a). The same age intervals are obtained when the dating is performed by marginalization, i.e., by estimating the posterior distribution of ages for this mean value incorporated in the data compilation used for curve calculation ([850 - 843 BCE] & [838 -758 BCE], Fig. 7b; Livermore et al., 2018; see also Gallet et al., 2020; Genevey et al., 2021).

In the next step, we conducted correlation dating for the individual intensity values obtained for each pottery fragment (Fig. 8a). It should be stressed that, in this case, the data considered are heterogeneous, since we are comparing data obtained at fragment level (those from Hama) and data averaged at the fragment group level used to calculate the reference curve (Livermore et al., 2021; Shaar et al., 2022). Despite this lack of homogeneity, which affects the statistical significance of the dating results obtained, it is noteworthy that all fragments, except for one (K122), are dated to a period earlier than 750 BCE. This indicates that the analyzed ceramics had been used for at least ~30 years at the time of the destruction of the city of Hama. This finding is quite surprising as these ceramics are considered ordinary vessels typically used for every-day purposes, implying that their use-life duration could have been rather short. Additionally, they were found in royal or other important architectural contexts, where presumably the replacement of common pottery would not have posed any financial or social difficulties.

At this stage of our study, two options of data interpretation are possible. The first option is that there is evidence suggesting a lengthy use of common wares, which would

make their archaeomagnetic analysis particularly challenging due to their variable firing dates relative to a well-defined event (in this case, the destruction of Hama). The second option is to question, to some extent, the reliability of the reference intensity variation curve for the specific period under consideration.

Here we explore the second possibility. Both the archaeointensity data from the destruction layers at Tel Megiddo and Tel Hazor dated to 732 BCE and the Hama destruction level dated to 720 BCE raise the same question regarding the duration of use of the analyzed common ceramics. To better understand the sensitivity of the intensity variation curve for these data points from Tel Megiddo and Tel Hazor (three for each site), we decided to remove them when calculating the average intensity variation curve. The resulting curve, shown in Fig. 6b (Table S4), reveals that the intensity maximum initially dated to the beginning of the second half of the 8th century has now shifted to the transition between the 8^{th} and 7^{th} centuries BCE. In this revised curve, the 8^{th} century is characterized by a single trend of increasing intensity, with a lower rate of change (maximum of ~0.2 μT/yr) compared to the previously observed rate during its first half (~0.5 μT/yr; Shaar et al., 2022). Additionally, the decreasing rate during the first half of the 7^{th} century BCE as seen in the original curve (Fig. 6a) is higher in the revised curve.

It is notable that the Hama data appear to be more consistent with this version of the reference intensity variation curve (Fig. 6b). The correlation dating of the mean value derived from all fragment data results in a 95%-probability time interval that almost includes the date of Hama's destruction (Fig. 9). This is also the case, relative to 732 BCE, for the three Tel Hazor data (fragment groups referred to as HZ05B, HZ05C; HZ06; Shaar et al., 2022) and two of the three values determined at Tel Megiddo (mgh03-low and mgq02; Fig. 9). Only the high intensity value of fragment group mgh03 (mgh03-high) from Tel Megiddo does not align with this pattern, suggesting a significantly different age for this group of four potsherds,

370 either older, around the second half of the 9th century BCE, or slightly younger, around 700
371 BCE. At this point, we can only speculate. If the first possibility suggests an extended use of
372 these ceramics, the second possibility indicates that they may have been accidentally
373 introduced into the archaeological level where they were found, possibly during leveling work
374 required for the site's reoccupation shortly after its destruction in 732 BCE. Further
375 discussion of this matter is beyond the scope of our study.

376 Continuing with the revised version of the intensity variation curve presented in Fig.
377 6b, correlation dating of the intensity values obtained for the Hama potsherds indicates that 11
378 out of 16 ceramics could be dated within a period of 30 years before the destruction of Hama
379 in 720 BCE, while the others would have had a longer use-life. Furthermore, six ceramics
380 could have been produced shortly before this destruction event (Fig. 8b). Such a relative
381 chronology can also be illustrated by calculating sliding averages from the values obtained for
382 three fragments, starting with the three highest values and gradually replacing the highest
383 value of the three data points (Fig. 10). Initially, the dating is compatible with the date of 720
384 BCE (upper diagram in Fig. 10b), but as the corresponding fragments are gradually replaced,
385 the dates shift towards the first half of the 8th century BCE. Unless this shift is attributed to the
386 experimental data dispersion, we favor the interpretation that it primarily indicates that the
387 analyzed ceramics were produced over a period of several decades, between ~800 and ~720
388 BCE. This suggests the possibility of tracking intensity variations during this time interval
389 and establishing a temporal order for these ceramics. Therefore, the alternative version of the
390 reference geomagnetic field intensity variation curve during the 8th century BCE, which
391 addresses the issue of the long use-life of the common pottery found in the 720 BCE
392 destruction level of Hama, warrants further analysis.

393 Finally, we compared the new archaeointensity results obtained at Hama with data
394 previously obtained from Qatna (Tell Mishrifeh), located ~35 km to the southeast, which

included fragments of large storage jars found in an agricultural storage complex that was likely also destroyed during the military campaign of Sargon II in 720 BCE (Gallet and al-Maqdissi, 2010; Livermore et al., 2021; see also al-Maqdissi, 2003; al-Maqdissi and Bonacossi, 2005). This comparison thus involves ceramics with potentially different lifespans. Given the nature of the ceramics at Qatna and their presumed longevity of use, a dating interval of 100 years (between 820 and 720 BCE) was defined by Livermore et al. (2021), in contrast to the narrower interval of 20 years initially considered by Gallet and al-Maqdissi (2010). On average, jars with handles exhibit higher archaeointensity values than those without, while all the results obtained at the fragment level display a similar scatter to that of the Hama data, also at the fragment level (Fig. S5). One possible interpretation is that the Hama data at the fragment level reflect a continuum between the two mean intensity values determined at Qatna. Jars with handles may have been produced shortly before the destruction in 720 BCE, while those without handles could have been produced several decades earlier. It is important to acknowledge that this interpretation is not exclusive and remains statistically fragile. However, it illustrates the richness of the discussions between archaeomagnetists and archaeologists, which intensify as we make progress in determining the reference geomagnetic field intensity variation in the Near East or other regions.

5. Concluding remarks

The destruction layers punctuating the occupation of ancient settlements are invaluable for archaeointensity studies as they provide ceramic fragments, often in large quantities, within a temporal context that is archaeologically homogeneous and potentially well dated, if the destruction event is historically known. Our study shows that this homogeneity is far from achieved when examining pottery, even common ceramics that are expected to have a relatively short use-life (see also Shaar et al., 2016).

The archaeointensity results obtained from 16 fragments (77 specimens) of different serving vessels intended for everyday use found in the 720 BCE Hama destruction layer yield a broad range of values, from ~65 μT to ~81 μT. We attribute this dispersion primarily to the different production dates of these ceramics during the 8th century BCE, a period characterized by rapid intensity fluctuations according to the currently available reference geomagnetic field intensity variation curve for the Near East (Shaar et al., 2022). This allows us to place them within a chronology relative to each other based on their manufacture (firing) dates.

Perhaps the most intriguing result obtained at Hama is that, using the established reference curve, the studied ceramics had been in use for at least 30 years by the time Hama was destroyed in 720 BCE. This is especially noteworthy considering that they were all found in royal and other important contexts where they presumably could have been easily replaced. The long use-life of the serving vessels is extremely interesting for the discussion of daily work-practices and economic sustainability of households (in this case, a large household), which should be explored further, but is beyond the scope of the paper. This time lag, along with the dispersion of archaeointensity values, makes the study of pottery from destruction layers particularly challenging from an archaeomagnetic standpoint due to dating uncertainties. However, we show that this lag could be due to inaccuracies in the reference intensity variation curve during the 8th century BCE, caused mainly by a limited archaeointensity dataset obtained on potsherds from Tell Megiddo in the Southern Levant. These fragments, also from common ceramic wares, share a similar archaeological context to those from Hama, namely a destruction layer.

From a methodological aspect, our study illustrates the potential of using pottery from a destruction layer to retrieve rapid variations in geomagnetic field intensity, as well as to

444 establish, through archaeomagnetic intensity-based dating, a comparative chronological order
445 of ceramics found in an otherwise chaotic context.

446

447 **Acknowledgements**

448 This research was supported by the Independent Research Fund Denmark for the project
449 "Ordinary Lives in Extraordinary Times: A New View of the Earliest Urban Societies in
450 Bronze Age Syria" (grant number 1024-00107B, award holder: Mette Marie Hald) and by the
451 Shelby White – Leon Levy Foundation for the project "Hama. City in the Upper Orontes
452 valley: Chronology and material Culture" led by Georges Mouamar. YG thanks Agnès
453 Genevey for fruitful discussions and help with this study, and Ron Shaar for his remarks on
454 the manuscript. YG also thanks Sylvie Froschl-Lejeune for stylistic improvements to the text,
455 and Maxime Le Goff for his invaluable help over the past 25 years. We are grateful to two
456 anonymous reviewers for their helpful comments.

457

458 **References**

459 al-Maqdissi, M., 2003. Recherches archéologiques syriennes à Mishirfeh-Qatna au nord-est
460 de Homs (émèse). Comptes Rendus des séances de l'Académie des Inscriptions et
461 Belles-Lettres, 147, pp. 1487–1515.

462 al-Maqdissi, M., Bonacossi, D.M., 2005. The Metropolis of the Orontes: Art and Archaeology
463 from the Ancient Kingdom of Qatna: Seven Years of Syrian-Italian Collaboration at
464 Mishrifeh-Qatna (Damascus).

465 Baaklini, A.-A., 2019. Présence et influence assyrienne dans le royaume de Hamat. Ph-D
466 Thesis, Doctoral School IV, Sorbonne Université, 661 pp.

467 Botta, P. E., Flandin, E., 1849. Monument de Ninive, vol. 1. Paris: Imprimerie nationale,
468 France.

469 Brown, M. C., Donadini, F., Korte, M., Nilsson, A., Korhonen, K., Lodge, A., et al., 2015.
470 GEOMAGIA50.v3: 1. general structure and modifications to the archeological and
471 volcanic database. Earth Planets and Space 67, 1-31.

472 Brown, M., Hervé, G., Korte, M., Genevey, A., 2021. Global archaeomagnetic data: the state-
473 of-the-art and future challenges. Phys. Earth Planet. Inter., 318, 106766.

474 Fugmann, E., 1958. Hama, Fouilles et recherches 1931-1938. II. L'architecture des périodes
475 pré-Hellénistiques. Fondation Carlsberg, Copenhagen Nationalmuseet Pub., 283 pp.

476 Gallet, Y., Genevey, A., Le Goff, M., Fluteau, F., Eshragi, S. A., 2006. Possible impact of the
477 Earth's magnetic field on the history of ancient civilizations. Earth Planet. Sci. Lett.
478 246, 17-26.

479 Gallet, Y., Le Goff, M., 2006. High-temperature archeointensity measurements from
480 Mesopotamia. Earth Planet. Sci. Lett. 241(1-2), 159-173

481 Gallet, Y., al-Maqdissi, M., 2010. Archeomagnetism in Mishrifeh-Qatna: New data on the
482 evolution of intensity in the earthly magnetic field in the Middle East during the last
483 millenia. Akkadica 131(1), 29-46.

484 Gallet, Y., Fortin, M., Fournier, A., Le Goff, M., Livermore, P., 2020. Analysis of
485 geomagnetic field intensity variations in Mesopotamia during the third millennium BC
486 with archeological implications. Earth Planet. Sci. Lett. 537, 116183.

487 Gallet, Y., 2021. The dawn of archeomagnetic dating. C. R. Geoscience 353 (1), 285-296.

Gallet, Y., Fournier, A., Livermore, P.W., 2021. Tracing the geomagnetic field intensity variations in Upper Mesopotamia during the Pottery Neolithic to improve ceramic-based chronologies. J. Archaeol. Sci. 132, 105430.

Gallet, Y., Le Goff, M., Genevey, A., 2022. Triaxe archeointensity analysis. Phys. Earth Planet. Inter. 332, 106924.

Gallet, Y., Le Goff, M., 2023. A complementary, two-method spherical approach to direction-based archeomagnetic dating. J. Archaeol. Sci. 152, 105743.

Genevey, A., Gallet, Y., Constable, C., Korte, M., Hulot, G., 2008. ArcheoInt: An upgraded compilation of geomagnetic field intensity data for the past ten millennia and its application to the recovery of the past dipole moment. Geochem. Geophys. Geosys. 9(4), Q04038.

Genevey, A., Gallet, Y., Rosen, J., Le Goff, M., 2009. Evidence for rapid geomagnetic field intensity variations in Western Europe over the past 800 years from new archeointensity French data. Earth Planet. Sci. Lett. 284, 132–143.

Genevey, A., Gallet, Y., Thébault, E., Livermore, P. W., Fournier, A., Jesset, S., Lefèvre, A., Mahé-Hourlier, N., Marot, E., Regnard, S., 2021. Archeomagnetic intensity investigations of French medieval ceramic workshops: Contribution to regional field modeling and archeointensity dating. Phys. Earth Planet. Inter. 318, 106750.

Hartmann, G.A., Genevey, A., Gallet, Y., Trindade, R.I.F., Etchevarne, C., Le Goff, M., Afonso, M.C., 2010. Archeointensity in Northeast Brazil over the past five centuries. Earth Planet. Sci. Lett. 296, 340–352.

Hartmann, G., Genevey, A., Gallet, Y., Trindade, R., Le Goff, M., Najjar, R., Etchevarne, C., Afonso, M., 2011. New historical archeointensity data from Brazil: Evidence for a large

regional non-dipole field contribution over the past few centuries. Earth Planet. Sci. Lett. 306, 66-76.

Hervé, G., Lanos, P., 2017. Improvements in Archaeomagnetic Dating in Western Europe from the Late Bronze to the Late Iron Ages: An Alternative to the Problem of the Hallstattian Radiocarbon Plateau. Archaeometry 60 (4), 870-883.

Ingholt, H., 1934. Rapport préliminaire sur la première campagne de fouilles de Hama. København, Levin & Munksgaard.

Ingholt, H., 1940. Rapport préliminaire sur sept campagnes de fouilles à Hama en Syrie (1932-1938). København, E. Munksgaard.

Le Goff, M., Gallet, Y., Genevey, A., Warmé, N., 2002. On archaeomagnetic secular variation curves and archaeomagnetic dating. Phys. Earth Planet. Inter. 134, 203-211.

Le Goff, M., Gallet, Y., 2004. A new three-axis vibrating sample magnetometer for continuous high-temperature magnetization measurements: applications to paleo- and archeo-intensity determinations. Earth Planet. Sci. Lett. 229, 31-43.

Livermore, P.W., Fournier, A., Gallet, Y., Bodin, T., 2018. Transdimensional inference of archeomagnetic intensity change. Geophys. J. Int. 215, 2008-2034.

Livermore, P.W., Gallet, Y., Fournier, A., 2021. Archeomagnetic intensity variations during the era of geomagnetic spikes in the Levant. Phys. Earth Planet. Inter. 312, 106657.

Lowrie, W., 1990. Identification of ferromagnetic minerals in a rock by coercivity and unblocking temperatures properties. Geophys. Res. Lett.17, 159–162

Lumsden, S., 2019. The Urban Topography of Iron Age Hama. In: Karlsson, M. (Ed.), The Rod and Measuring Rope: Festschrift for Olof Pedersén. Wiesbaden: Harrasowitz Verlag, pp. 58-81.

534 Pavón-Carrasco, F. J., Rodríguez-González, J., Osete, M. L., Torta, J. M., 2011. A matlab tool
535 for archeomagnetic dating. J. Archeol. Sci. 38 (2), 408–419.

536 Riis, P.J., Buhl, M.-L., 1990. Hama, Fouilles et Recherches, 1931-1938; II, 2. Les objets de la
537 période dite syro-hittite (Âge du Fer). Nationalmuseets Skrifter, Større Beretninger, 12.
538 Copenhagen: National Museum of Denmark.

539 Schnepp, E., Obenaus, M., Lanos, P., 2015. Posterior archaeomagnetic dating: An example
540 from the Early Medieval site Thunau am Kamp, Austria. Journal of Archaeological
541 Science: Reports 2, 688-698.

542 Shaar, R., Tauxe, L., Ron, H., Ebert, Y., Zuckerman, S., Finkelstein, I., Agnon A., 2016.
543 Large geomagnetic field anomalies revealed in Bronze to Iron Age archeomagnetic data
544 from Tel Megiddo and Tel Hazor, Israel. Earth Planet. Sci. Lett. 442, 173-185.

545 Shaar, R., Bechar, S., Finkelstein, I., Gallet, Y., Martin, M. A. S., Ebert, Y., Keinan, J.,
546 Gonen, L., 2020. Synchronizing geomagnetic field intensity records in the Levant
547 between the 23rd and 15th centuries BCE: chronological and methodological
548 implications. Geochem. Geophys. Geosyst. 21, e2020GC009251.

549 Shaar, R. Gallet, Y., Vaknin, Y., Gonen, L., Martin, M.A.S., Finkelstein, I, 2022.
550 Archaeomagnetism in the Levant and Mesopotamia reveals the largest changes in the
551 geomagnetic field. J. Geophys. Res.: Solid Earth 127, e2022JB024962.

552 Shahack-Gross, R., Shaar, R., Hassul, E., Ebert, Y., Forget, M., Nowaczyk, N., Marco, S.,
553 Finkelstein, I., Agnon, A., 2018. Fire and collapse: Untangling the formation of
554 destruction layers using archaeomagnetism. Geoarchaeology 33 (5), 513-528.

555 Troyano, M. Gallet, Y., Genevey, A., Pavlov, V., Fournier, A. Lagroix, F., Niyazova, M.,
556 Mirzaakhmedov, D., 2021. Analyzing the geomagnetic axial dipole field moment over

the historical period from new archeointensity results at Bukhara (Uzbekistan, Central Asia). Phys. Earth Planet. Inter. 310, 106633.

Vaknin, Y., Shaar, R., Gadot, Y., Shalev, Y., Lipschits, O., Ben-Yosef, E., 2020. The Earth's magnetic field in Jerusalem during the Babylonian destruction: A unique reference for field behavior and an anchor for archaeomagnetic dating. PloS ONE 15, e0237029..

Vaknin, Y., Shaar, R., Lipschits, O., Mazar, A., Maeir, A., Garfinkel, Y., et al., 2022. Reconstructing biblical military campaigns using geomagnetic field data. Proceedings of the national Academy of Sciences 119 (44).

566

567 **Figure captions**

568 **Fig. 1.** a) Photo of the mound at Hama in the 1930s. b) Destruction layer of Phase E in Room
569 V of Building II. @ National Museum of Denmark.

570 **Fig. 2.** Examples of pottery analyzed in this study. @ Georges Mouamar.

571 **Fig. 3.** Examples of thermal demagnetization and archaeointensity results obtained for four
572 different pottery specimens using the experimental protocol developed for the Triaxe
573 magnetometers. On the left, thermal demagnetization data is presented, while on the right, the
574 R(Ti), R'(Ti) and AutoR'(Ti) data (white, blue and red dots, respectively) obtained for the
575 corresponding specimens are shown. See the text, Le Goff and Gallet (2004) and Gallet et al.
576 (2022) for a detailed description of these parameters.

577 **Fig. 4.** Archaeointensity results obtained from R'(Ti) data of six different pottery fragments
578 (one diagram per fragment). Each curve exhibits the series of R'(Ti) values obtained for the
579 same specimen (see Table S1); their average, for the selected range of temperatures, gives the
580 archaeointensity value for each specimen. These values are then considered to calculate a
581 mean intensity value per fragment. Data from the ten other fragments are shown in Fig. S4.

582 **Fig. 5.** Average archaeointensity values obtained for each of the 16 suitable potsherds, with
583 their finds context. The diagram on the right shows the histogram of these archaeointensities.

584 **Fig. 6.** Evolution of geomagnetic field intensities (scale to the left) and corresponding Virtual
585 Axial Dipole Moments (VADM; scale to the right) in the Near East during the first half of the
586 1st millennium BCE calculated from the Bayesian AH-RJMCMC method (Livermore et al.,
587 2018), using (a) the data compilation made by Shaar et al. (2022), and (b) this compilation
588 after exclusion of the Tel Megiddo and Tel Hazor data dated around 732 BCE (see text). All
589 archaeointensity data were transferred to the latitude of Hama (λ = 35° 08' 07.5'') . The

590 computational parameters are as follows: $\sigma_{move} = 30$ years, σ_{change} and $\sigma_{birth} = 5\ \mu$T, $K_{max} = 150$,
591 a chain length of 200 million samples, priors of 20 μT and 110 μT for the minimum and
592 maximum intensities, and one datum age perturbed per age-resampling step. The probability
593 densities are reported in greyscale, with darker shades for higher probabilities. The blue thin
594 dashed lines indicate the 95%-credible interval and the thick blue line shows the median
595 curve (see Tables S3 and S4, respectively). The open and closed red symbols exhibit the
596 Hama data at the fragment level and the mean intensity value determined from all fragments,
597 respectively.

598 **Fig. 7.** Archaeomagnetic dating of the mean archaeointensity value determined from all the
599 Hama fragments. (a) Correlation dating considering a time interval between 850 and 720
600 BCE. (b) Marginalization dating of the archaeointensity value with the same *a priori* dating
601 interval. The dating results are the same: [850 - 843 BCE] & [838 -758 BCE]. Probability
602 densities > 95.4% are shown in light blue. See the text, Livermore et al. (2018) and Genevey
603 et al. (2021) for more details.

604 **Fig. 8.** Archaeomagnetic correlation dating carried out for each of the 16 suitable pottery
605 fragments, considering an age interval between 850 and 720 BCE. (a), (b) the reference field
606 intensity evolution is that of Fig. 6a and Fig. 6b, respectively. Probability densities > 95.4%
607 are shown in light blue.

608 **Fig. 9.** Archaeomagnetic correlation dating of the Tel Hazor and Tel Meggido data (fragment
609 group level; three values each) removed from the compilation of Shaar et al. (2022) (see text),
610 as well as Hama data also at the fragment group level. The probability densities > 95.4% are
611 shown in green, red and blue, respectively.

612 **Fig. 10.** Correlation dating of running averages determined from groups of three intensity
613 values obtained at the fragment level in Hama. In each group, from top to bottom, the highest

614 value is replaced by the value immediately lower than the lowest value in the previous group.
615 The time interval tested is between 800 and 720 BCE. a) Intensity values of the different
616 groups relative to the intensity variation curve shown in Fig. 6b (see text). b) Probability
617 density of the dating of the different groups, using the same color code as in diagram (a). The
618 groups of three fragments used for the calculations are indicated on the right of the diagram.

619 **Table 1.** New archaeointensity data acquired at the fragment level from 16 distinct vessels
620 found in the destruction layer of Hama dated to 720 BCE.

621

622 **Supplementary information**

623 **Fig. S1.** The mound of Hama and the layout of the main buildings of Phase E mentioned in
624 the text (Fugmann, 1958).

625 **Fig. S2.** Three examples of heating and cooling susceptibility versus temperature curves
626 acquired up to 620°C and the isothermal remanent magnetization (IRM) acquisition curves up
627 to 1.5 T for the 16 fragments analyzed in our study. The insets in the susceptibility diagrams
628 show the heating and cooling susceptibility versus temperature curves acquired at maximum
629 temperatures similar to those considered for archaeointensity determination. Magnetic
630 susceptibility and IRM measurements were carried out using a KLY3 kappabridge coupled
631 with a CS3 furnace (AGICO) and a Vibrating Sample Magnetometer (VSM) model 3900,
632 respectively.

633 **Fig. S3.** Examples of thermal demagnetization of three-axis isothermal magnetization (IRM)
634 acquired on cubic (1cm-side) samples in fields of 1.5 T (red triangles), 0.4 T (green squares)
635 and 0.2 T (blue dots). Each sample comes from a different fragment. IRM experiments were
636 carried out using a MMPM10 pulse magnetizer, and the magnetization components were
637 measured using a JR6 spinner magnetometer (AGICO).

Fig. S4. Archaeointensity results obtained from R'(Ti) data of ten different pottery fragments (one diagram per fragment). Each curve exhibits the series of R'(Ti) values obtained for the same specimen, their average, for the selected range of temperatures, gives the archaeointensity value for each specimen. These values are then considered to calculate a mean intensity value per fragment. See also Fig. 4 and Table S1.

Fig. S5. Distribution of the archaeointensity data at the pottery fragment level obtained at Hama (blue dots: common pottery, this study), and Qatna (red dots: storage jars without handles, Gallet et al-Maqdissi, 2010; red triangles: storage jars with four handles, Livermore et al., 2021).

Table S1. Series of R'(Ti) data obtained for all (77) specimens successfully analyzed from 16 potsherds. See Fig. 4 and S4.

Table S2. New archaeointensity data obtained at Hama both at the specimen and fragment levels.

Table S3. AH-RJMCMC-derived results used to plot the geomagnetic field intensity variation curve shown in Fig. 6a (LAC; Shaar et al., 2022 and see computational parameters in the caption of Fig. 6). The data compilation is that of Shaar et al. (2022). This file includes the median curve, the 95% confidence interval and the probability density distribution of intensities at each date between ~3000 and ~500 BCE.

Table S4. AH-RJMCMC-derived results used to plot the geomagnetic field intensity variation curve shown in Fig. 6b (see computational parameters in the caption of Fig. 6). Three data points from both Tel Megiddo and Tel Hazor were excluded from the data compilation by Shaar et al. (2022) (see text). This file presents the median curve, the 95% confidence interval and the probability density distribution of intensities at each date between ~3000 and ~500 BCE.

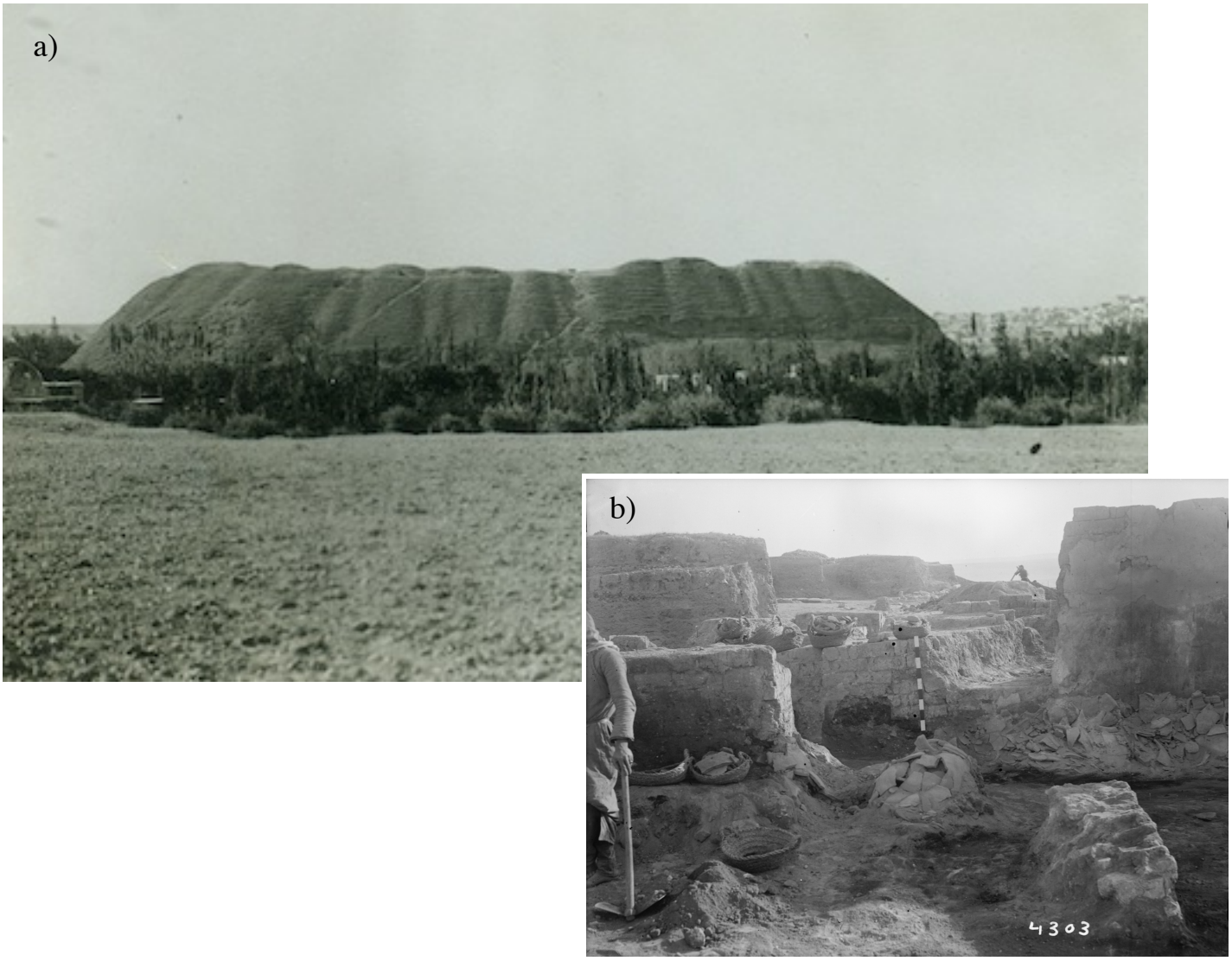

Figure 1

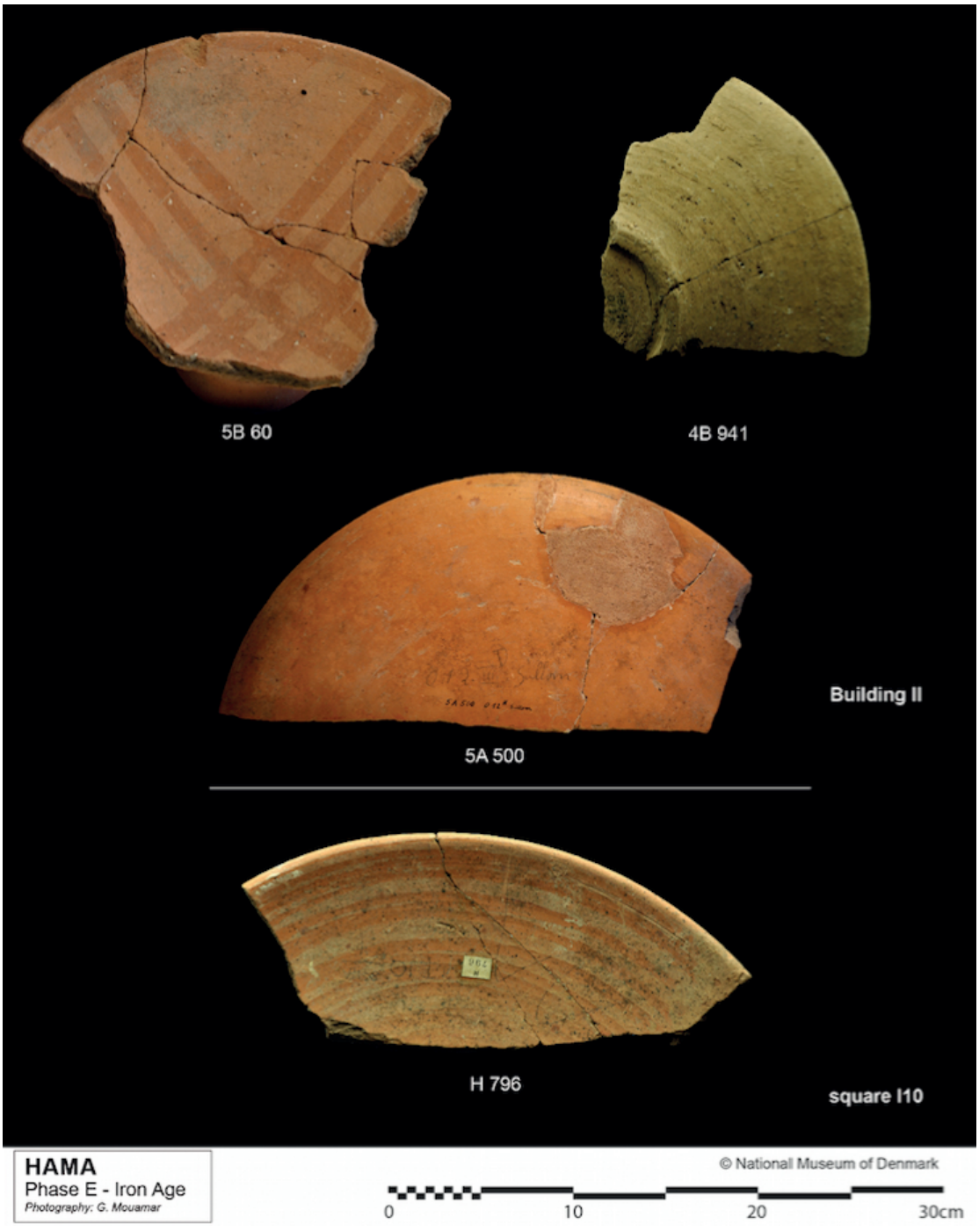
5B 60
4B 941
5A 500
Building II
H 796
square I10
HAMA
Phase E - Iron Age
Photography: G. Mouamar
© National Museum of Denmark
0
10
20
30cm

Figure 2

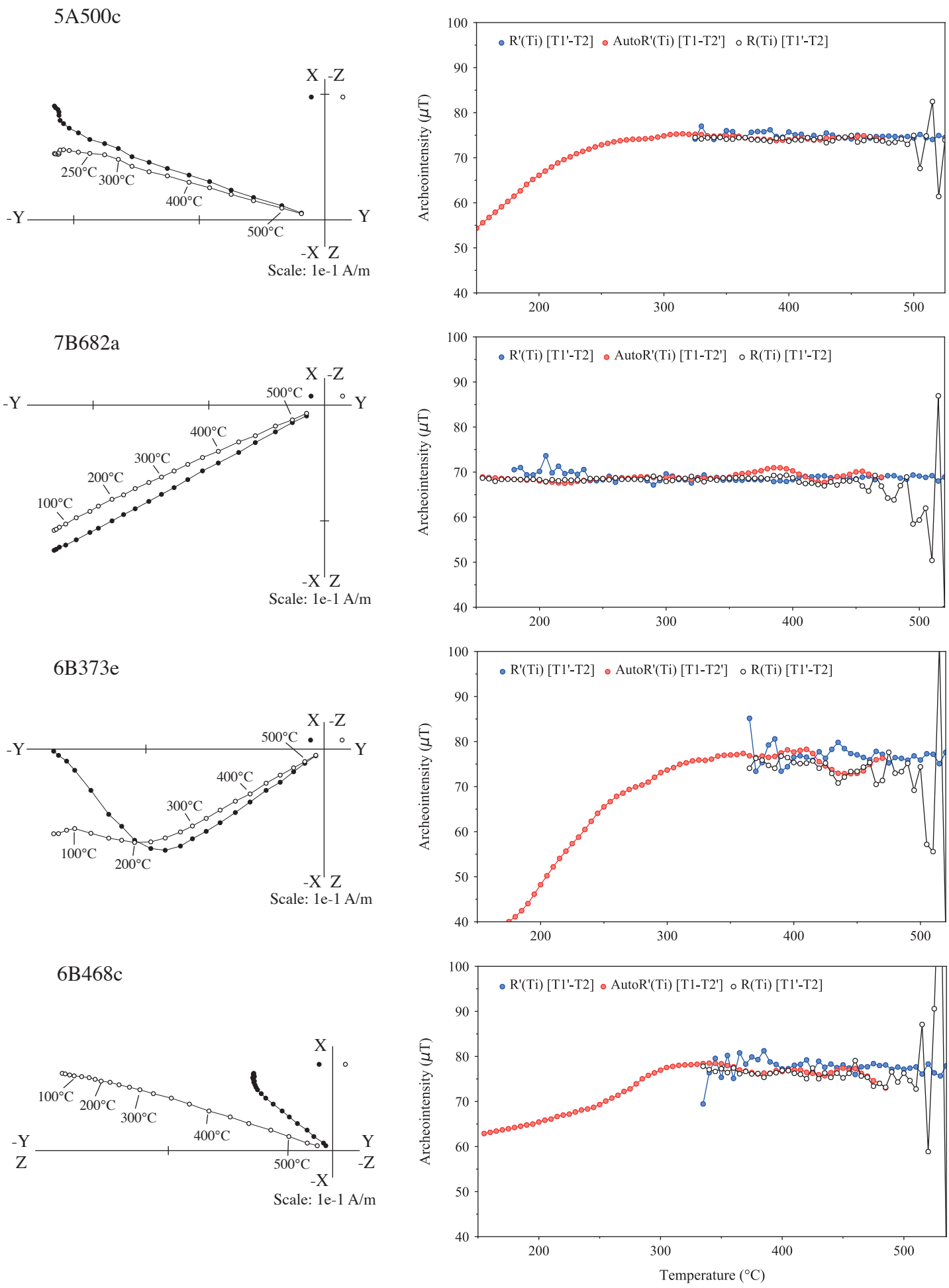
5A500c
X -Z
250°C
300°C
400°C
500°C
-Y
Y
-X Z
Scale: 1e-1 A/m
R'(Ti) [T1'-T2]
AutoR'(Ti) [T1-T2']
R(Ti) [T1'-T2]
Archeointensity (μT)
7B682a
100°C
200°C
300°C
400°C
500°C
6B373e
6B468c
Temperature (°C)

Figure 3

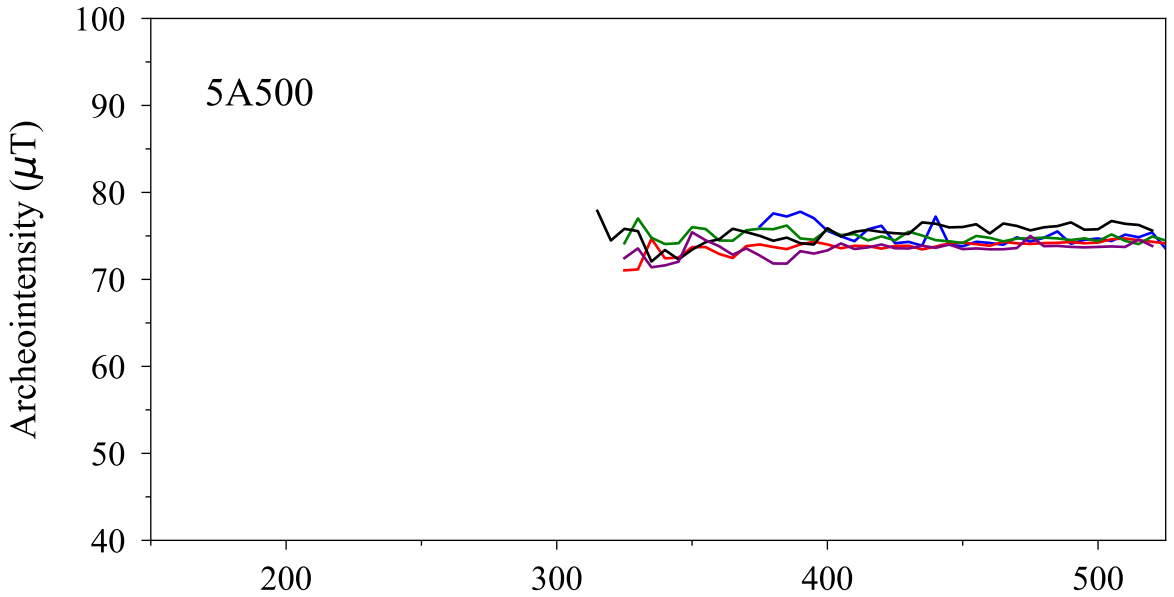
5A500
Archeointensity (μT)
100
90
80
70
60
50
40
200
300
400
500

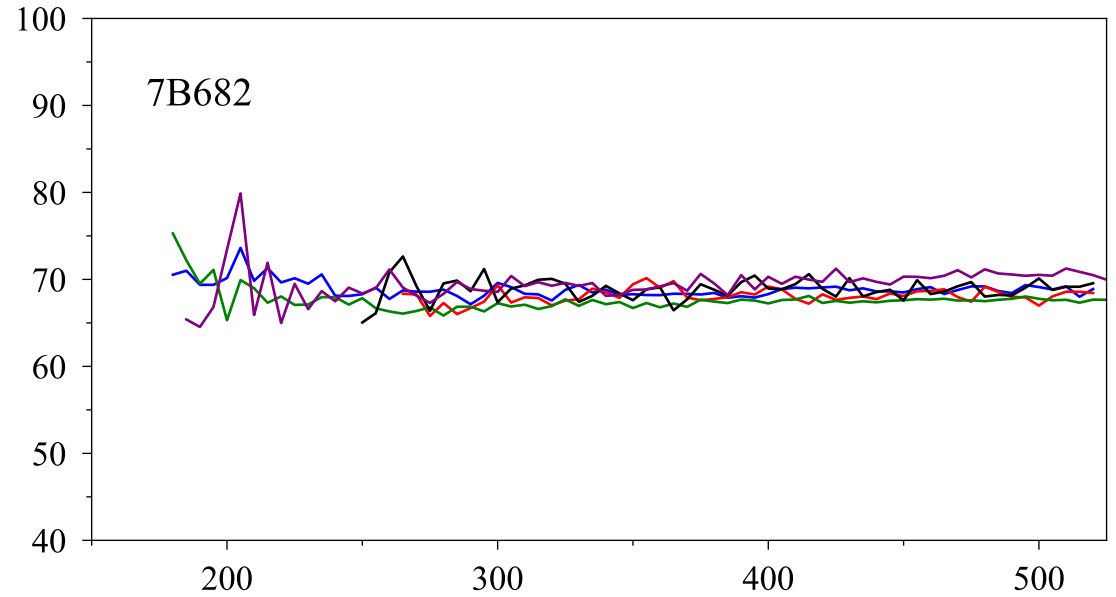
7B682
100
90
80
70
60
50
40
200
300
400
500

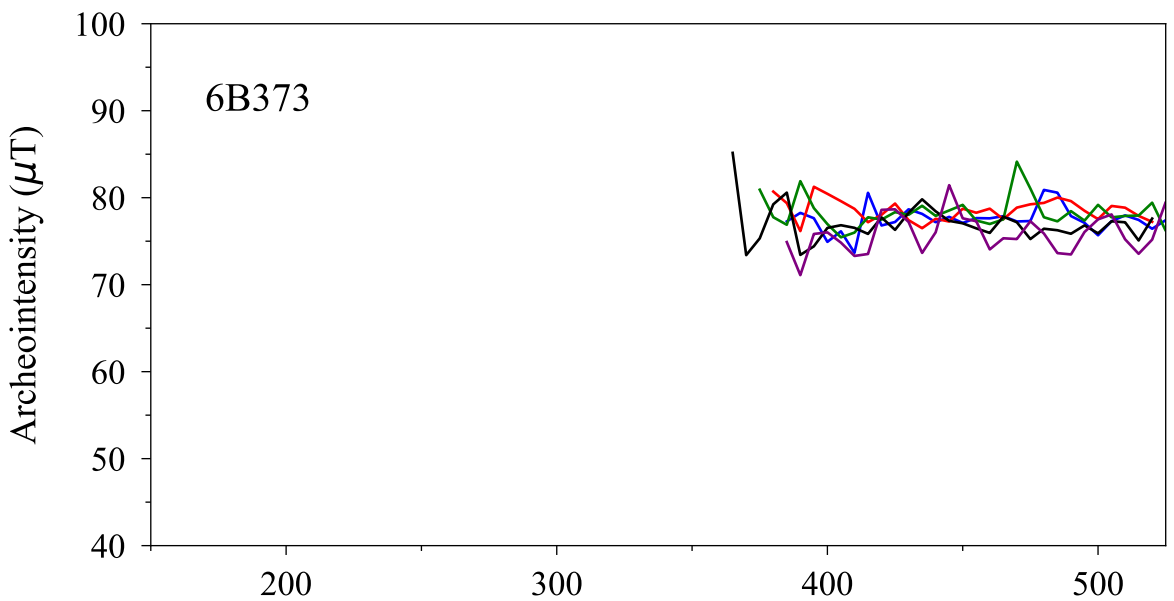
6B373
Archeointensity (μT)
100
90
80
70
60
50
40
200
300
400
500

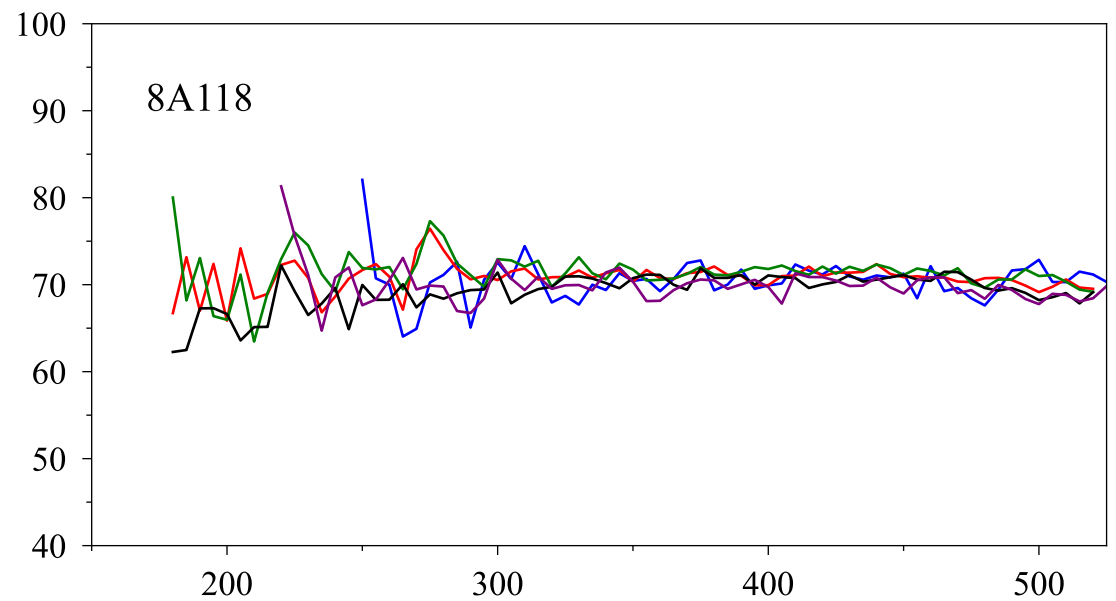
8A118
100
90
80
70
60
50
40
200
300
400
500

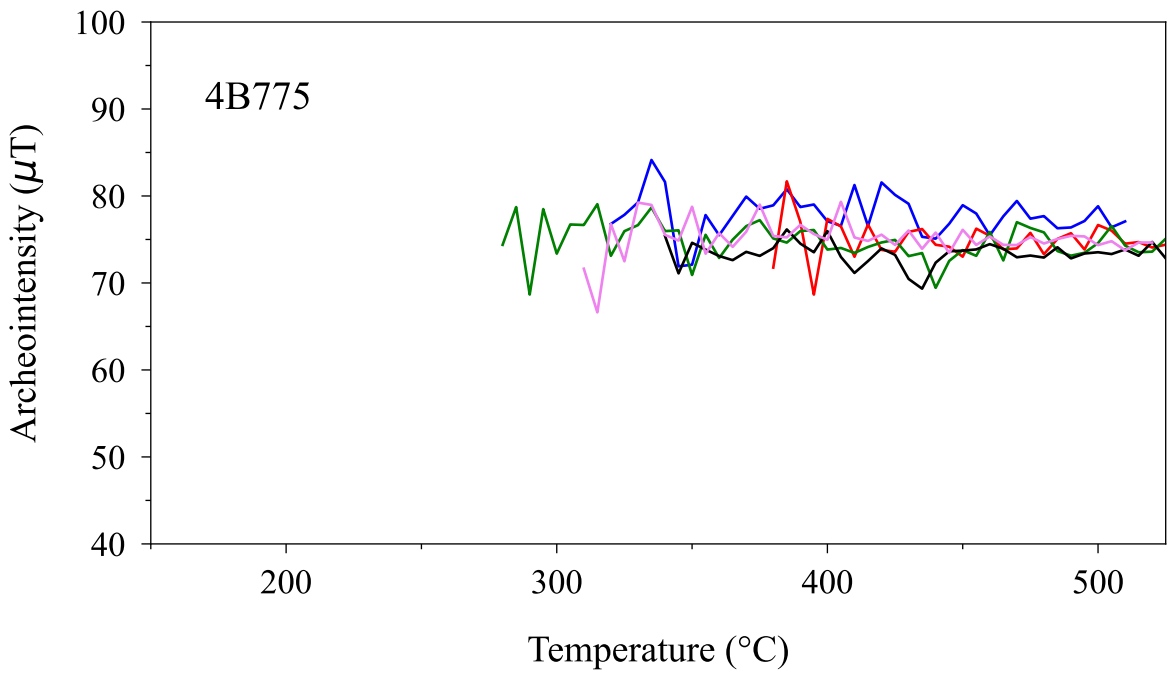
4B775
Archeointensity (μT)
100
90
80
70
60
50
40
200
300
400
500
Temperature (°C)

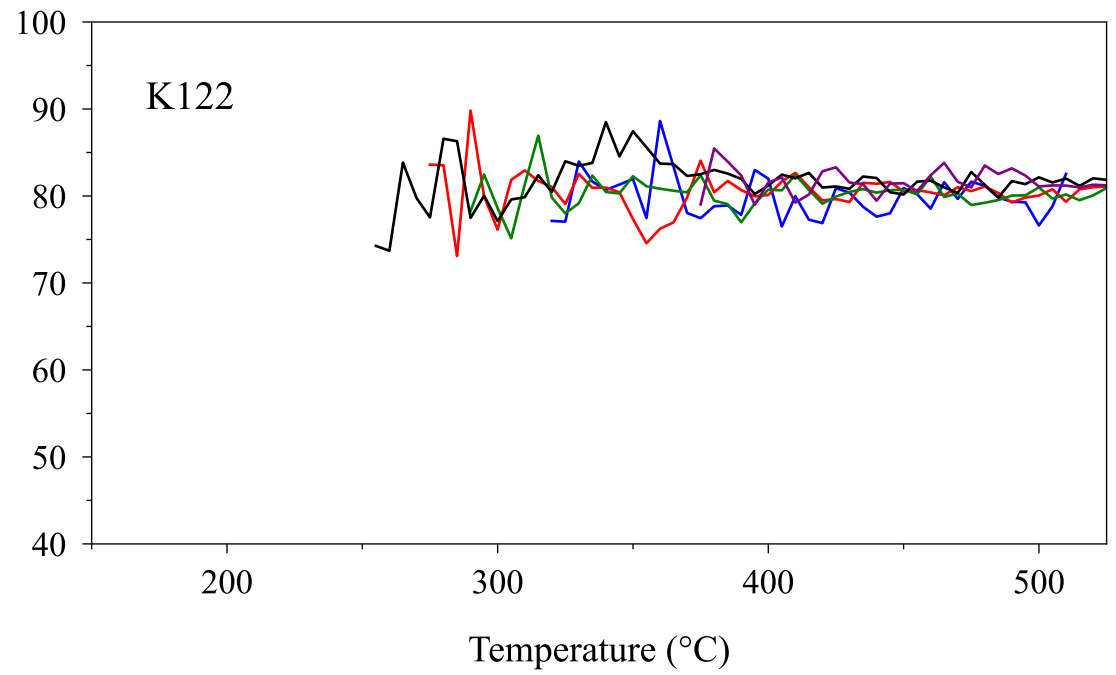
K122
100
90
80
70
60
50
40
200
300
400
500
Temperature (°C)

Figure 4

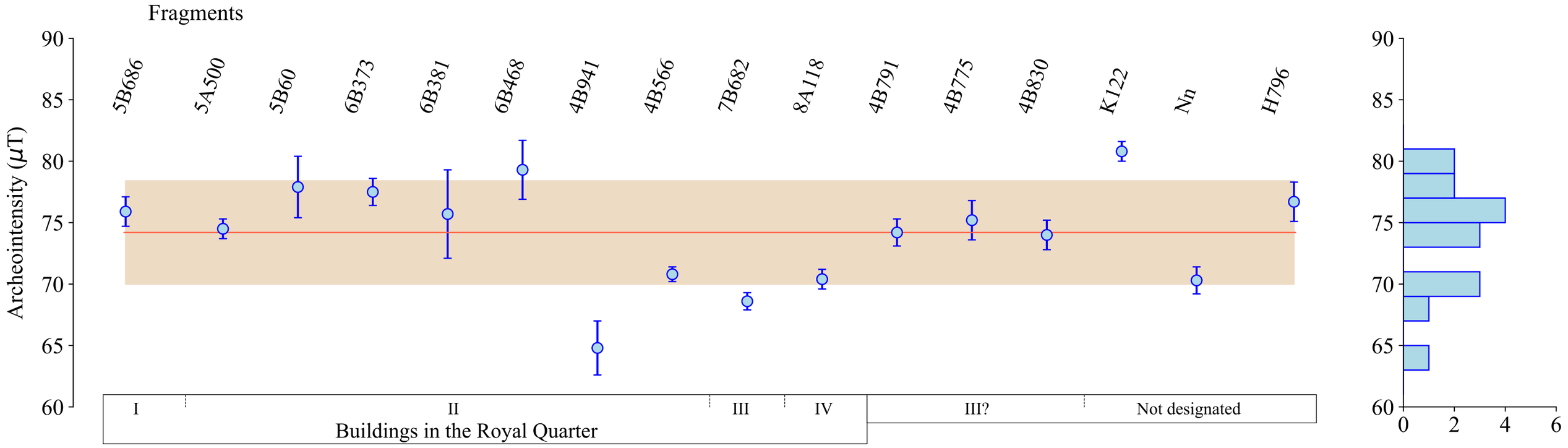
Fragments
Archeointensity (μT)
90
85
80
75
70
65
60
5B686
5A500
5B60
6B373
6B381
6B468
4B941
4B566
7B682
8A118
4B791
4B775
4B830
K122
Nn
H796
I
II
III
IV
III?
Not designated
Buildings in the Royal Quarter
Numbers
0
2
4
6

Figure 5

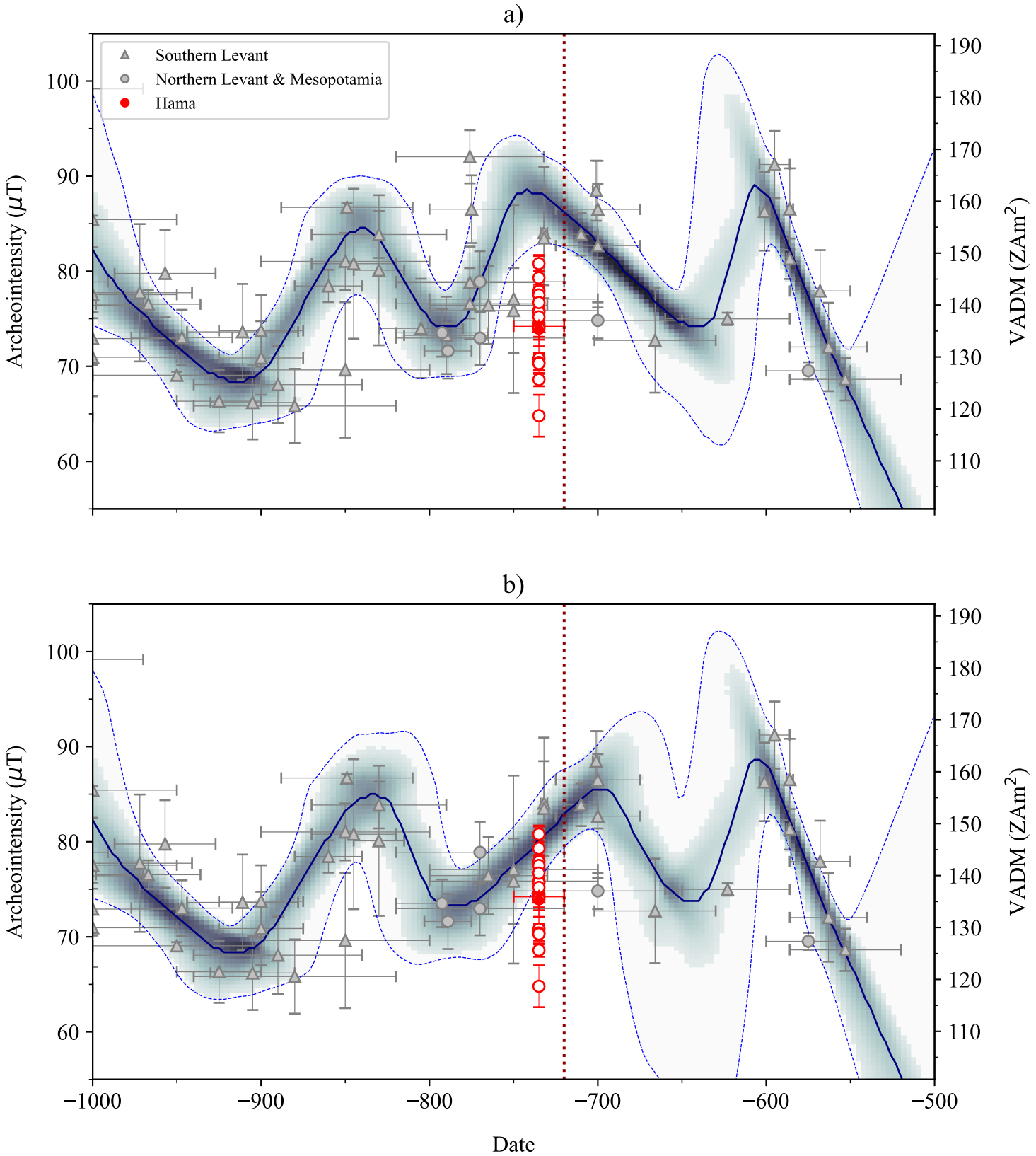
a)
Southern Levant
Northern Levant & Mesopotamia
Hama
Archeointensity (μT)
VADM (ZAm²)
b)
Archeointensity (μT)
VADM (ZAm²)
Date

Figure 6

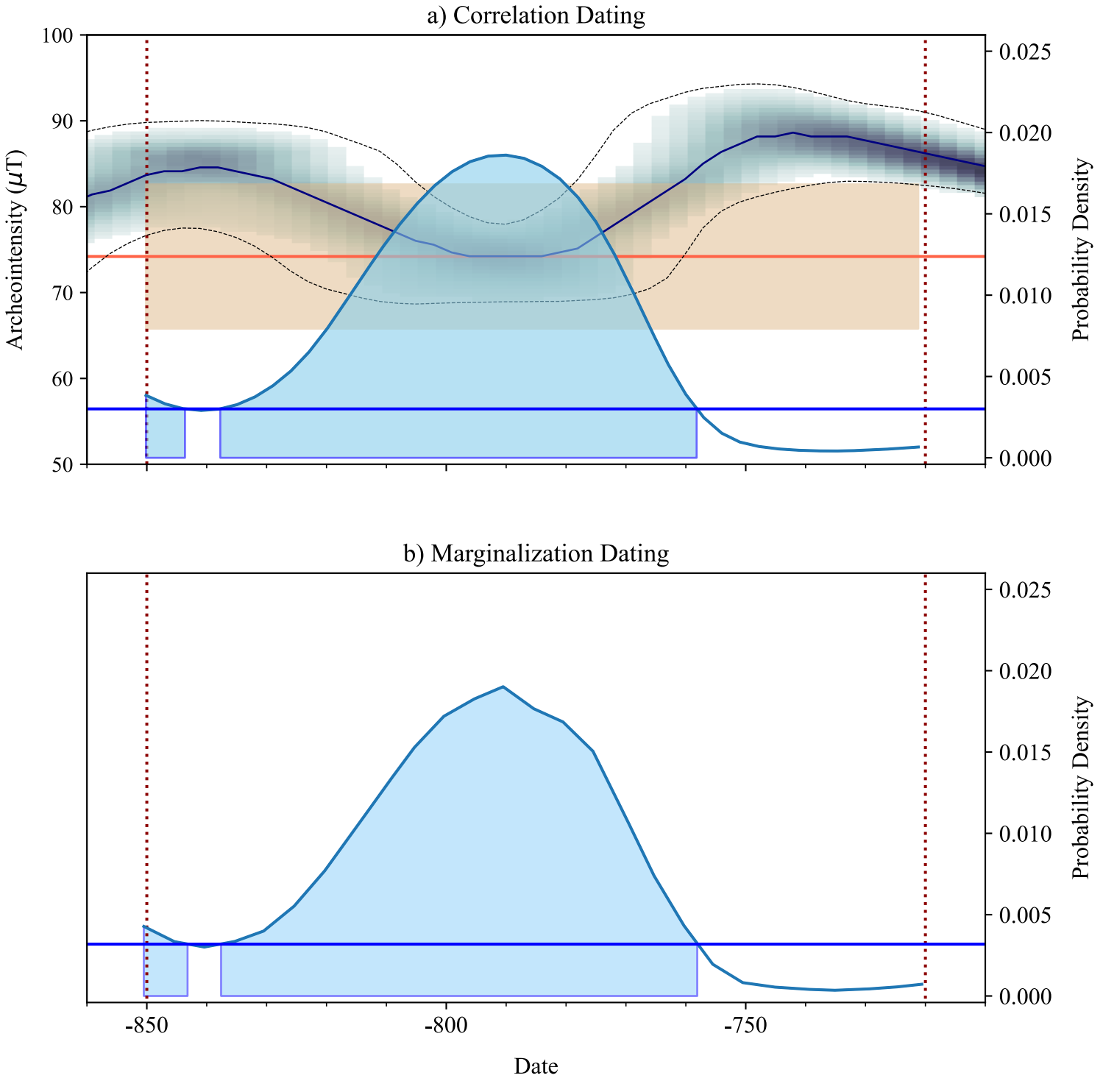
a) Correlation Dating
Archeointensity (μT)
100
90
80
70
60
50
0.025
0.020
0.015
0.010
0.005
0.000
Probability Density
b) Marginalization Dating
Probability Density
-850
-800
-750
Date

Figure 7

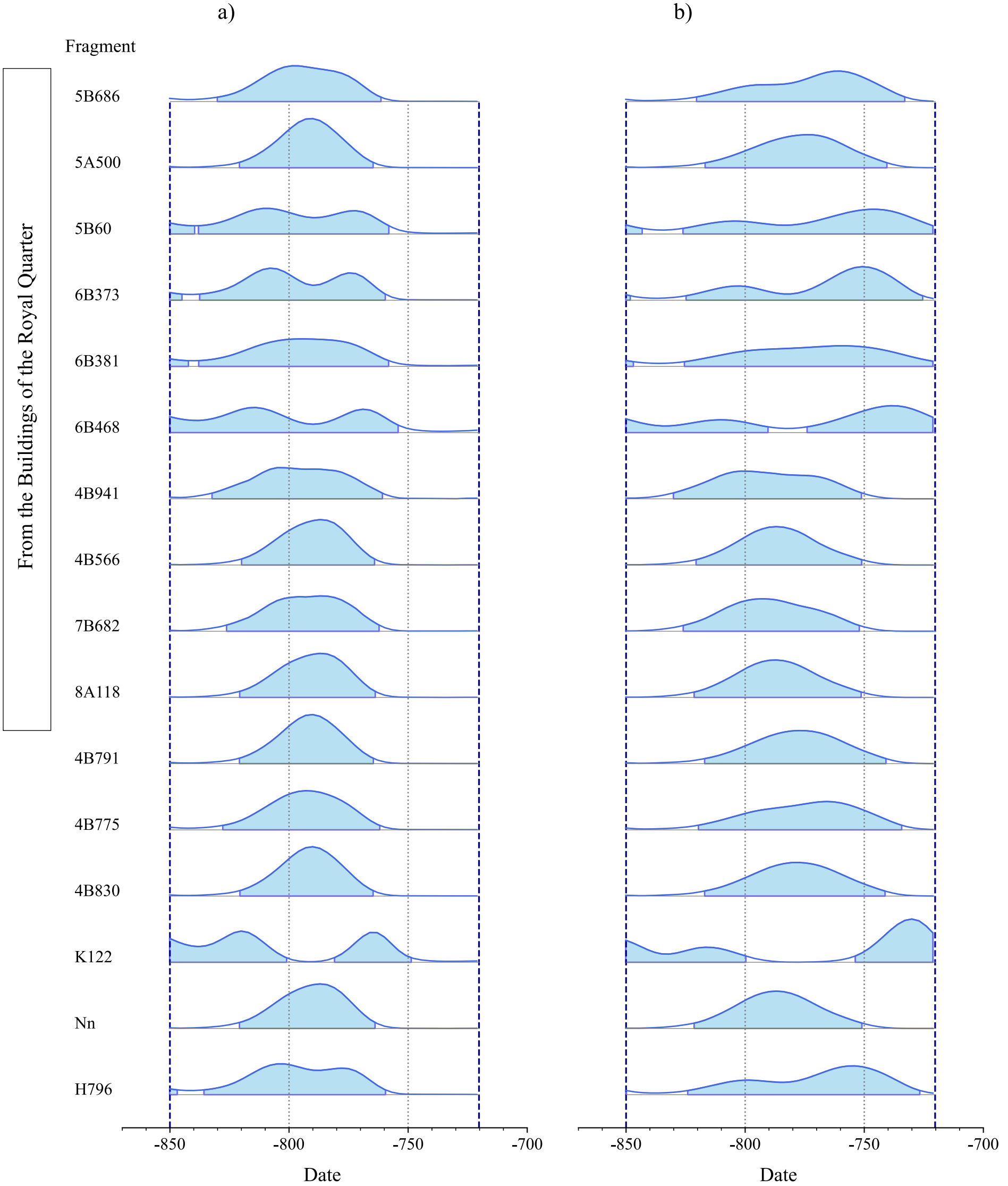
a)
b)
Fragment
From the Buildings of the Royal Quarter
5B686
5A500
5B60
6B373
6B381
6B468
4B941
4B566
7B682
8A118
4B791
4B775
4B830
K122
Nn
H796
-850
-800
-750
-700
Date
-850
-800
-750
-700
Date

Figure 8

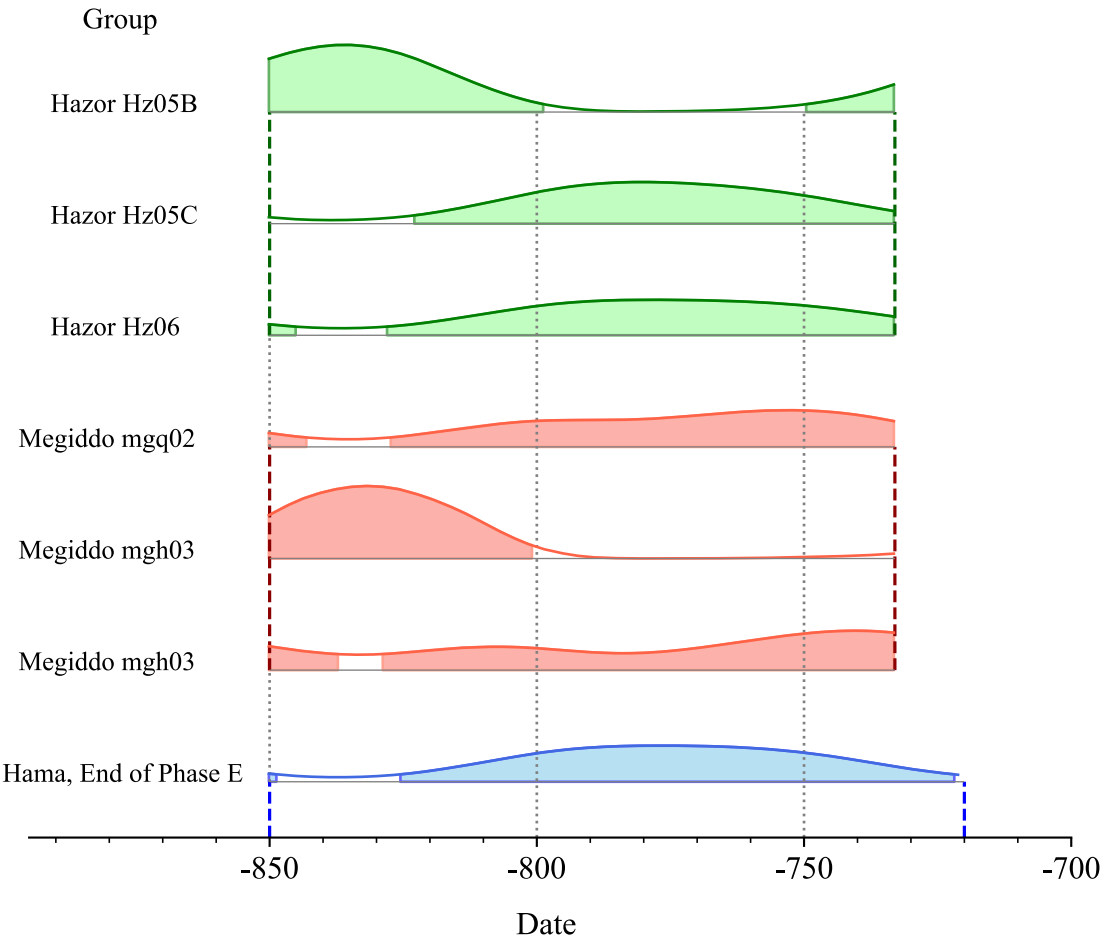
Group
Hazor Hz05B
Hazor Hz05C
Hazor Hz06
Megiddo mgq02
Megiddo mgh03
Megiddo mgh03
Hama, End of Phase E
-850
-800
-750
-700
Date

Figure 9

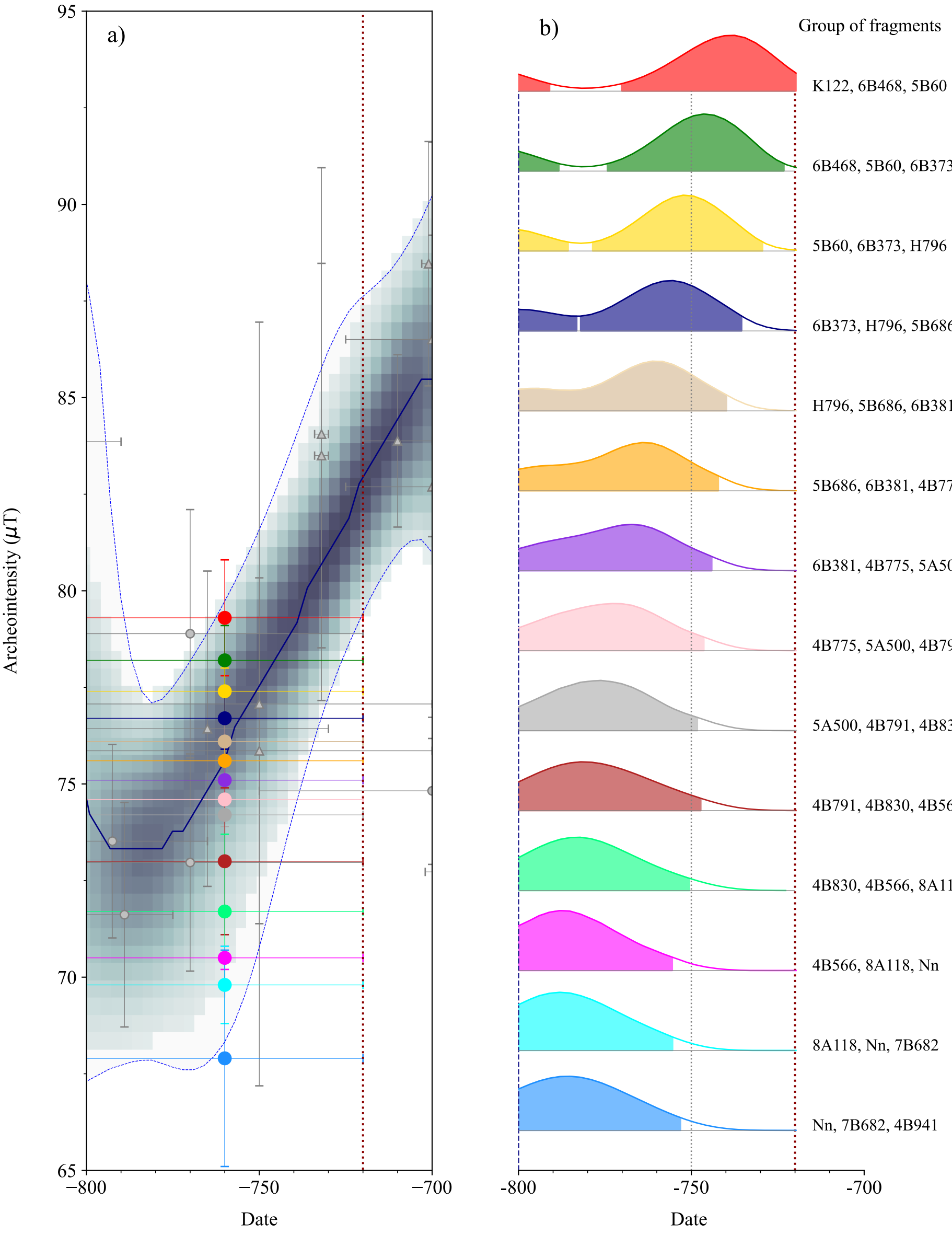
a)
b)
Group of fragments
K122, 6B468, 5B60
6B468, 5B60, 6B373
5B60, 6B373, H796
6B373, H796, 5B686
H796, 5B686, 6B381
5B686, 6B381, 4B775
6B381, 4B775, 5A500
4B775, 5A500, 4B791
5A500, 4B791, 4B830
4B791, 4B830, 4B566
4B830, 4B566, 8A118
4B566, 8A118, Nn
8A118, Nn, 7B682
Nn, 7B682, 4B941
Archeointensity (μT)
95
90
85
80
75
70
65
−800
−750
−700
-800
-750
-700
Date
Date

Figure 10

Archeol. Context	Fragment	Use of ceramics	Number of specimens	F fragment ± σ (μT)	F group ± σ (μT)
Buildings, Royal Quarter					
Building I, Room D	5B686	serving vessel	4	75.9 ± 1.2	
Building II, Sillom D	5A500	serving vessel	5	74.5 ± 0.8	
Building II, Room T/K	5B60	serving vessel	5	77.9 ± 2.5	
Building II, Room N	6B373	serving vessel	5	77.5 ± 1.1	
Building II, Room D	6B381	serving vessel	5	75.7 ± 3.6	
Building II, Room D	6B468	serving vessel	5	79.3 ± 2.4	
Building II, O12X	4B941	serving vessel	5	64.8 ± 2.2	
Building II, O12X	4B566	medium-sized jar	5	70.8 ± 0.6	
Building III, N14	7B682	serving vessel	5	68.6 ± 0.7	
Building IV, Room A	8A118	serving vessel	5	70.4 ± 0.8	
Other Buildings					
K15 X	4B791	medium-sized jar	5	74.2 ± 1.1	
K15 VII	4B775	serving vessel	5	75.2 ± 1.6	
K15 IX	4B830	serving vessel	3	74.0 ± 1.2	
H10	K122	serving vessel	5	80.8 ± 0.8	
I11	Nn	serving vessel	5	70.3 ± 1.1	
I10	H796	serving vessel	5	76.7 ± 1.6	
					74.2 ± 4.2

Table 1

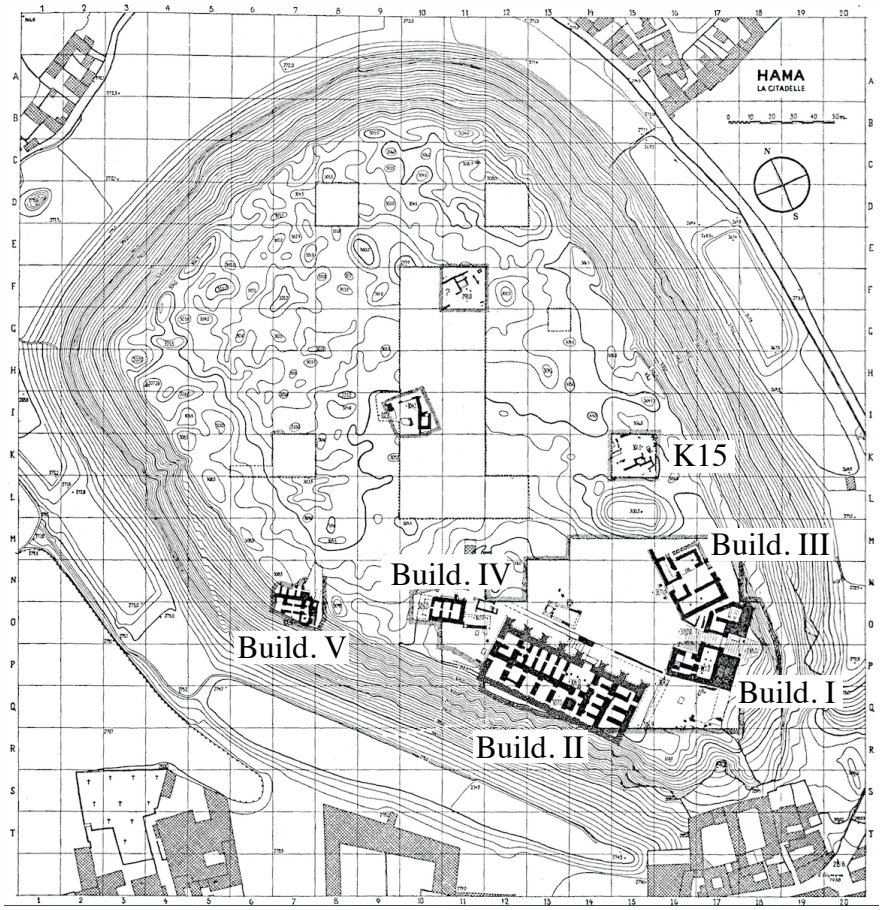
HAMA
LA CITADELLE
K15
Build. III
Build. IV
Build. V
Build. I
Build. II

Figure S1

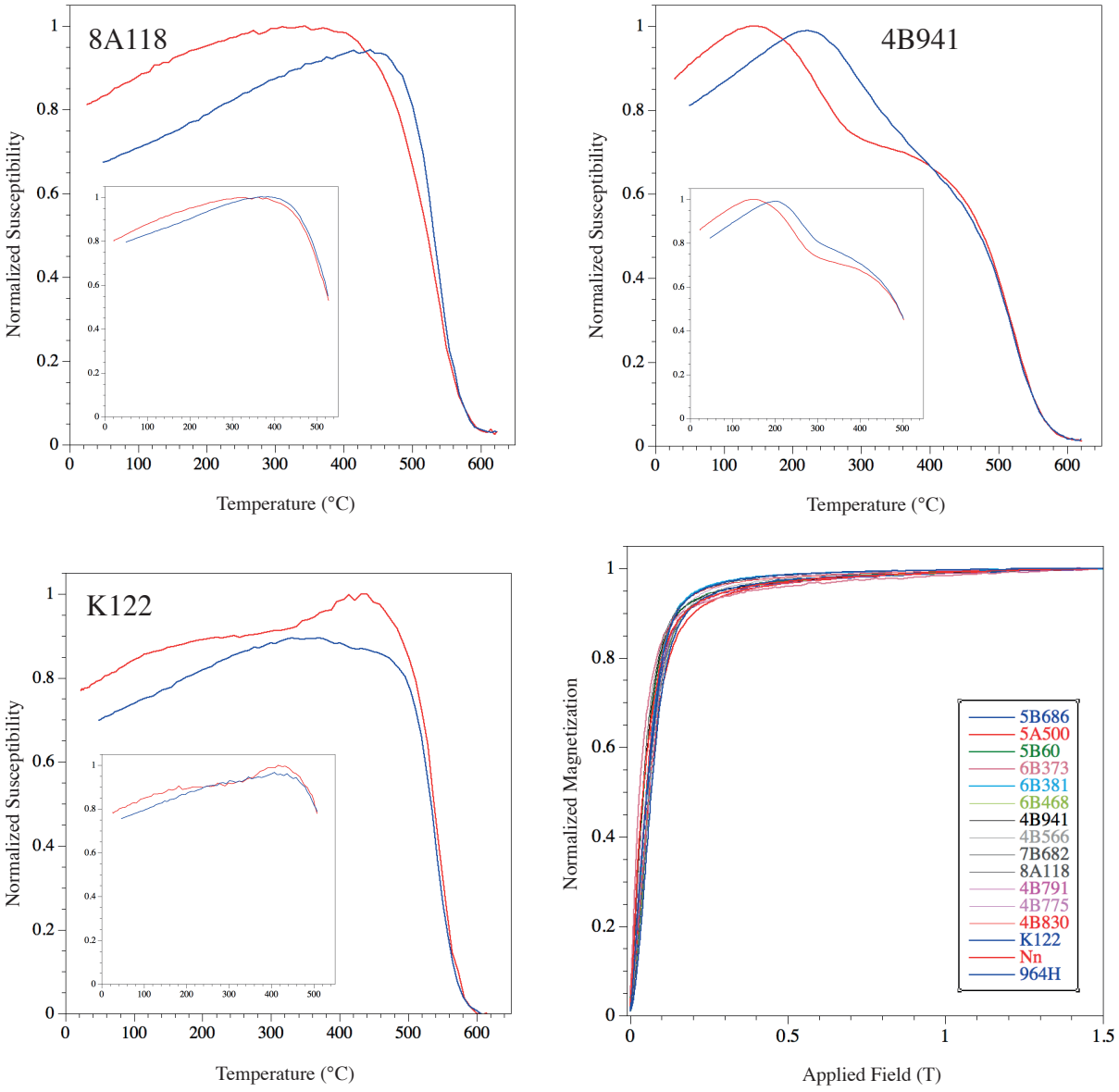
8A118
4B941
K122
Normalized Susceptibility
Temperature (°C)
Normalized Magnetization
Applied Field (T)
5B686
5A500
5B60
6B373
6B381
6B468
4B941
4B566
7B682
8A118
4B791
4B775
4B830
K122
Nn
964H

Figure S2

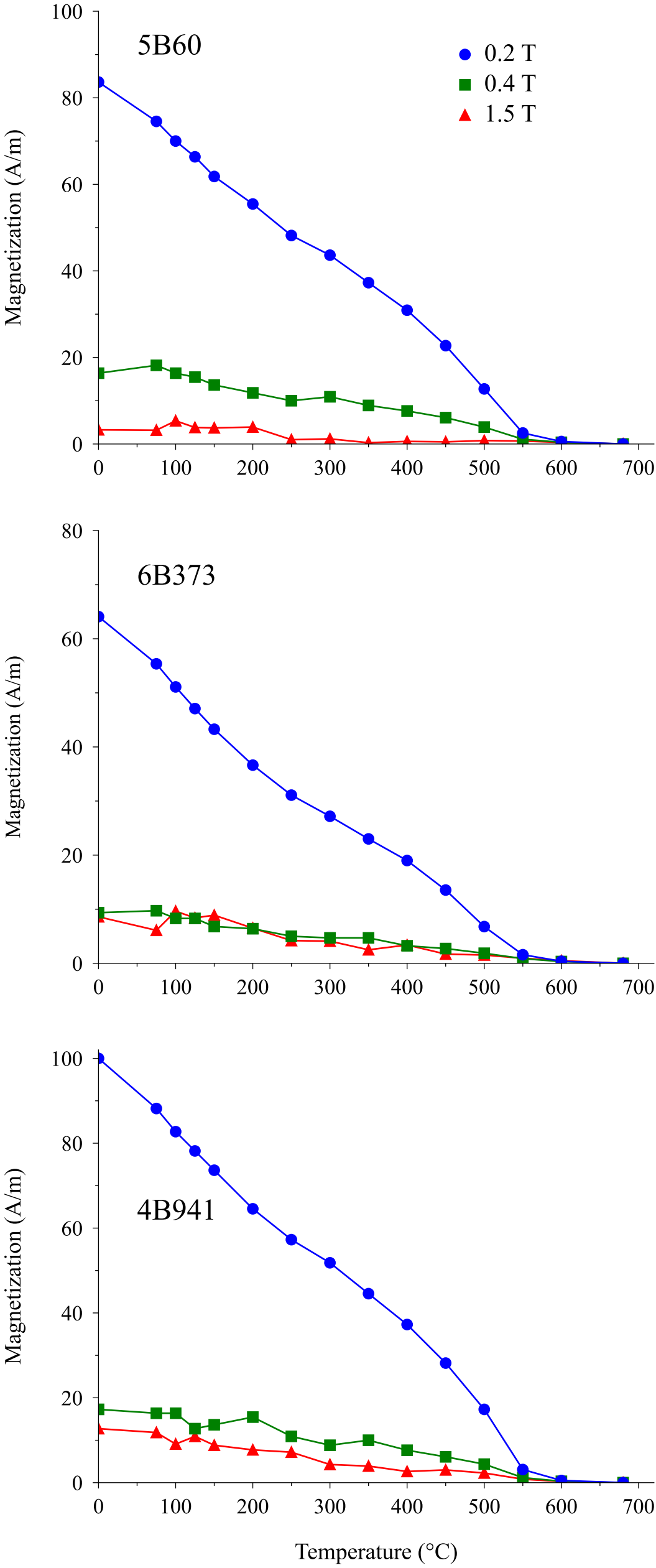
5B60
0.2 T
0.4 T
1.5 T
Magnetization (A/m)
0
20
40
60
80
100
0
100
200
300
400
500
600
700
6B373
Magnetization (A/m)
0
20
40
60
80
0
100
200
300
400
500
600
700
4B941
Magnetization (A/m)
0
20
40
60
80
100
0
100
200
300
400
500
600
700
Temperature (°C)

Figure S3

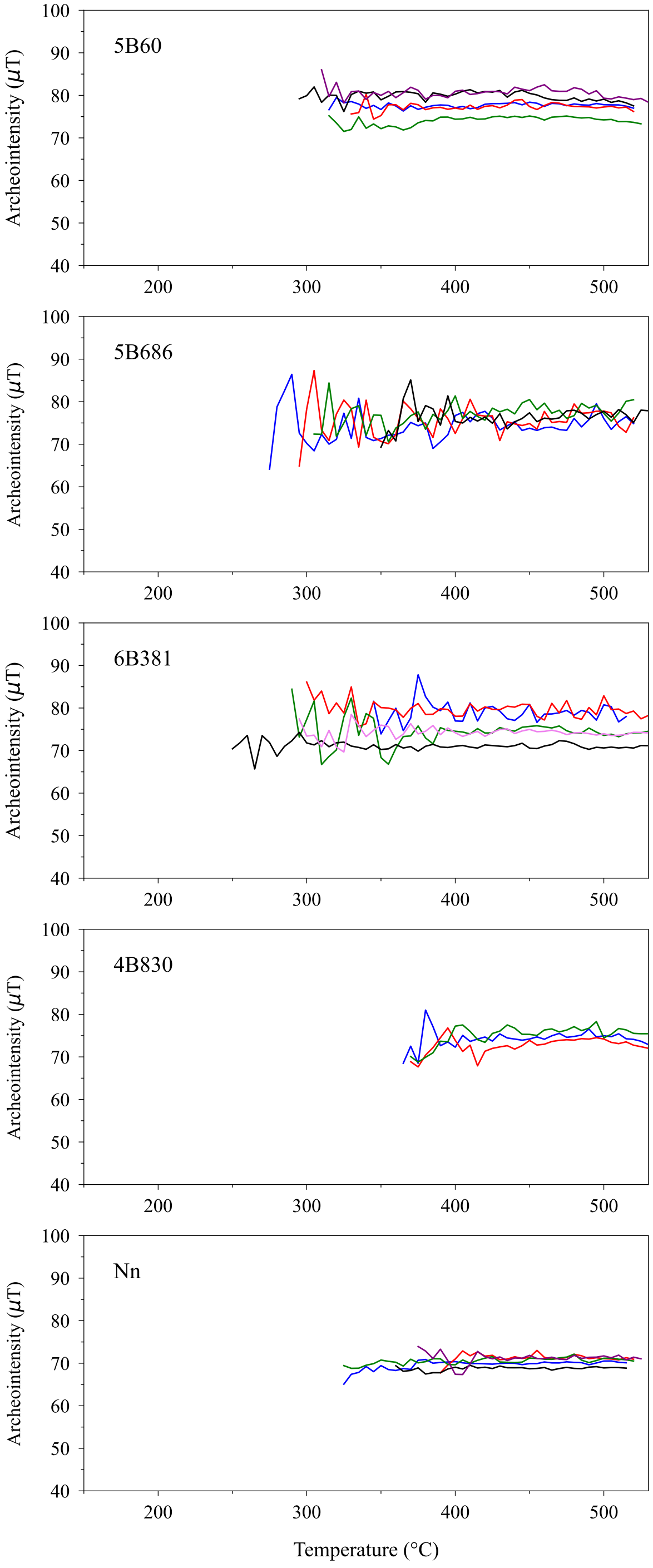
5B60
6B468
5B686
4B566
6B381
4B941
4B830
4B791
Nn
H796
Archeointensity (μT)
Temperature (°C)
100
90
80
70
60
50
40
200
300
400
500

Figure S4

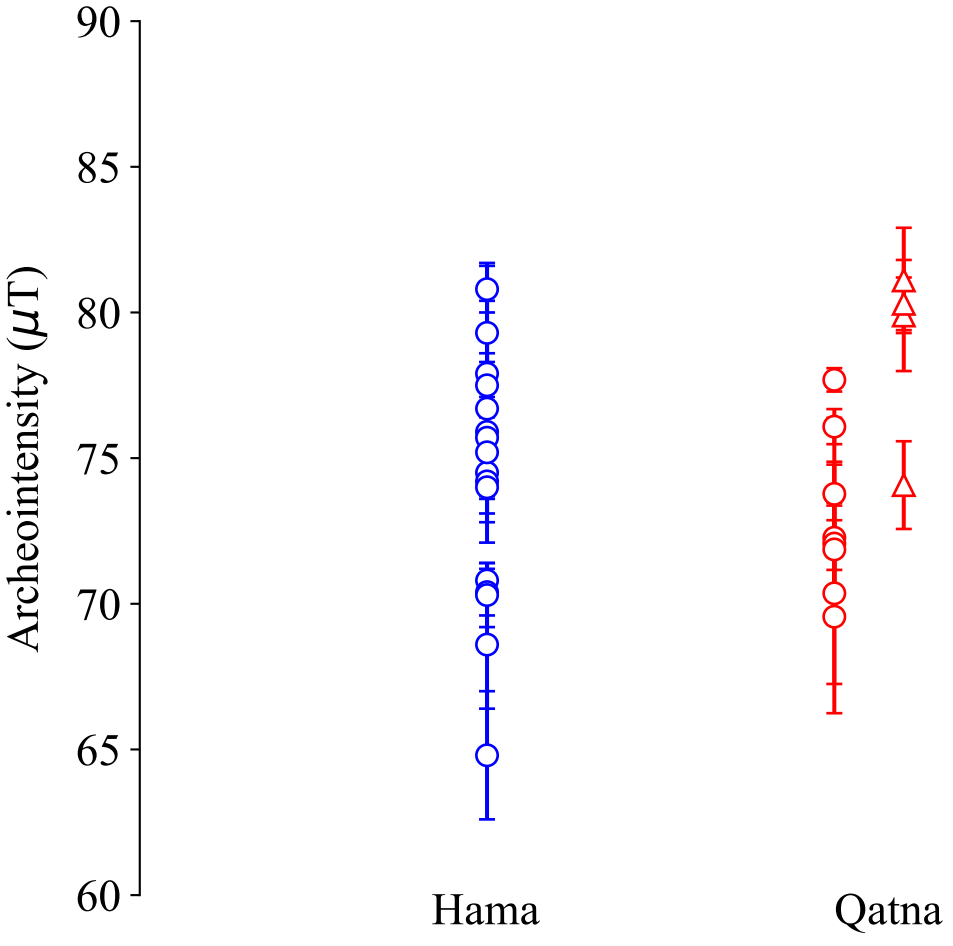

Figure S5

Table S2

Archeol. Context	Fragment	Specimen	T1'-T2 (°C)	Hlab (μT)	NRM T1' (%)	Slope R' (%)	F specimen (μT)	F frag ± σ (μT)
Buildings, Royal Quarter								
Building I, Room D	**5B686**	a	275 - 520	75	81	3	74.3	75.9 ± 1.2
		c	295 - 520	75	79	2	75.6	
		d	305 - 520	75	83	6	77.0	
		f	350 - 530	75	84	2	76.5	
Building II, Sillom D	**5A500**	a	375 - 525	75	72	-4	75.1	74.5 ± 0.8
		b	325 - 525	75	80	3	73.8	
		c	325 - 525	75	82	-1	74.9	
		d	315 -520	75	76	3	75.4	
		e	325 - 520	75	75	2	73.5	
Building II, Room T/K	**5B60**	b	315 - 520	75	83	0	77.7	77.9 ± 2.5
		c	330 - 520	75	82	1	77.3	
		d	315 - 525	75	88	2	74.1	
		e	295 - 520	75	88	-2	79.8	
		f	310 - 530	75	90	-2	80.6	
Building II, Room N	**6B373**	b	385 - 530	75	85	1	77.5	77.5 ± 1.1
		c	380 - 520	75	86	-1	78.6	
		d	375 - 530	75	85	0	78.3	
		e	365 - 520	75	84	-2	77.0	
		f	385 - 530	75	83	2	75.9	
Building II, Room D	**6B381**	a	345 - 515	75	57	-1	79.0	75.7 ± 3.6
		b	300 - 540	75	75	-3	79.7	
		c	290 - 540	75	81	-1	74.5	
		d	250 - 540	75	83	-1	71.1	
		e	295 - 540	75	81	0	74.2	
Building II, Room D	**6B468**	a	340 - 520	75	70	3	76.4	79.3 ± 2.4
		b	395 - 535	75	78	-2	80.3	
		c	335 - 535	75	80	0	77.7	
		d	415 - 540	75	84	0	82.6	
		e	400- 540	75	85	4	79.6	
Building II, O12X	**4B941**	a	180 - 520	70	80	-2	65.8	64.8 ± 2.2
		b	255 - 515	70	76	2	63.6	
		c	305 - 520	70	75	2	63.2	
		d	275 - 520	70	81	2	63.2	
		f	280 - 515	70	77	0	68.3	
Building II, O12X	**4B566**	a	285 - 510	75	57	-4	70.5	70.8 ± 0.6
		b	265 - 540	70	77	1	70.2	
		c	285 - 530	70	71	-1	70.4	
		e	275 - 535	70	73	1	71.1	
		f	300 - 535	70	75	-3	71.6	
Building III, N14	**7B682**	a	180 - 520	75	84	-2	68.9	68.6 ± 0.7
		b	265 - 520	75	77	1	68.1	
		d	180 - 530	70	86	-2	67.6	
		e	250 - 520	70	82	0	68.9	
		f	185 - 530	70	88	3	69.5	
Building IV, Room A	**8A118**	a	250 - 530	75	77	0	70.5	70.4 ± 0.8
		b	180 - 520	70	86	0	70.8	
		c	180 - 520	70	82	-1	71.4	
		d	180 - 520	70	87	6	69.2	
		e	220 - 530	70	87	-3	70.0	
Other Buildings								
K15 X	**4B791**	b	355 - 520	75	85	4	74.6	74.2 ± 1.1
		c	390 - 515	75	82	1	74.7	
		d	365 - 515	75	83	3	74.2	
		f	305 - 520	75	83	-4	75.3	
		g	365 - 520	75	83	7	72.4	
K15 VII	**4B775**	a	320 - 510	75	60	-2	77.9	75.2 ± 1.6
		c	380 - 530	75	73	-1	74.9	
		d	280 - 530	75	73	-2	74.8	

		e	340 - 525	75	66	0	73.4	
		f	310 - 520	75	65	0	75.2	
K15 IX	**4B830**	b	365 - 530	75	88	3	74.3	74.0 ± 1.2
		c	370 - 530	75	88	4	72.7	
		d	370 - 530	75	85	7	75.1	
H10	**K122**	a	320 - 510	75	61	-1	79.9	80.8 ± 0.8
		b	275 - 535	75	78	0	80.5	
		c	290 - 540	75	79	0	80.2	
		d	255 - 540	75	81	1	81.7	
		e	375 - 545	75	80	-1	81.6	
I11	**Nn**	a	325 - 515	75	87	4	69.6	70.3 ± 1.1
		b	390 - 520	70	83	1	71.3	
		c	325 - 520	70	84	2	70.5	
		d	360 - 515	70	83	1	68.8	
		e	375 - 525	70	81	0	71.2	
I10	**H796**	b	260 - 540	75	80	-1	77.0	76.7 ± 1.6
		c	220 - 530	75	77	-2	78.7	
		d	180 - 535	75	77	1	74.9	
		e	225 - 535	75	76	-2	75.4	
		f	245 - 535	75	75	1	77.5	